EXPLORING AND CORRECTING MOTION IN RESTING-STATE FUNCTIONAL MAGNETIC RESONANCE IMAGES OF CONGENITAL HEART DISEASE PATIENTS

by

Jenna Marie Schabdach

B. S. Electrical Engineering, Drexel University, 2016

M. S. Electrical Engineering, Drexel University, 2016

M. S. Biomedical Informatics, University of Pittsburgh, 2018

Submitted to the Graduate Faculty of

the Department of Biomedical Informatics in partial fulfillment

of the requirements for the degree of

Doctor of Philosophy

University of Pittsburgh

2019

UNIVERSITY OF PITTSBURGH

SCHOOL OF MEDICINE

This dissertation was presented

by

Jenna Marie Schabdach

It was proposed on

June 27, 2019

and approved by

Dr. Douglas Landsittal, Department of Biomedical Informatics

Dr. Ashok Panigrahy, Department of Biomedical Informatics

Dr. Gregory Cooper, Department of Biomedical Informatics

Dr. Rafael Ceschin, Department of Pediatric Radiology, Children's Hospital of Pittsburgh of UPMC

Dissertation Director: Dr. Douglas Landsittal, Department of Biomedical Informatics

EXPLORING AND CORRECTING MOTION IN RESTING-STATE FUNCTIONAL MAGNETIC RESONANCE IMAGES OF CONGENITAL HEART DISEASE PATIENTS

Jenna Marie Schabdach, PhD

University of Pittsburgh, 2019

Approximately 1.35 million children are diagnoses with a congenital heart defect (CHD) annually. As the process of diagnosing and treating CHD has improved, the expected lifespan of CHD patients has increased: at least 12 to 34 million adults worldwide have CHD. A larger population living with CHD means that clinicials are learning more about conditions which CHD patients are at increased risk of getting. Some of these conditions affect the patient's neurodevelopment and neurocognitive status. Diagnosis of the neurocognitive conditions is performed using surveys, but examining the structure and function of the brain could offer more objective diagnoses.

One tool useful for examining a patient's brain is magnetic resonance imaging (MRI). Resting state functional MRI (rs-fMRI) in particular can be used to reveal information about the neuronal networks in the patient's brain. Unfortunately, rs-fMRIs are highly susceptible to motion. Clinical and behavioral techniques can help patients move less during a rs-fMRI scan, though they do not guarantee motion-free images. Various sensors can be used to monitor and correct for motion during the scan, but these sensors are useless when it comes to recovering previously acquired rs-fMRIs corrupted by motion.

We devised a novel approach to volume registration, which is the first step in motion correction. We compare it to traditional volume registration in the context of a complete motion correction pipeline. The registration techniques and pipeline were applied to neurological rs-fMRIs of fetal, neonatal, preadolescent, and adult patients with CHD as well as

several phantom images. We identified different motion patterns specific to different demographic groups, and discovered relationships between certain motion patterns and clinical outcomes associated with CHD and different neurodevelopmental conditions.

TABLE OF CONTENTS

1.0 INTRODUCTION

Patient motion is a critical cause of data loss in medical imaging. Many approaches have been developed to prevent and reduce the impact of motion before, during, and after image acquisition. The effectiveness of these techniques vary between patient populations. If the effects of a patient's movements cannot be removed from an image, that image is considered to have been corrupted by motion and is deemed unusable.

Various clinical, behavioral, and technical protocols have been developed in an attempt to prevent patient motion from impacting the rs-fMR image as it is acquired. Sedation can be used to immobilize a patient during a scan, but requires additional personal to perform safely and involves a greater time commitment from the patient. Sedation is also not recommended for use in young children and fetal patients. Behavioral and educational techniques can be employed to prepare a patient for stressors he may experience during a medical imaging scan, but these approaches do not prevent the patient from moving out of boredom, discomfort, or distress. Several groups have developed techniques to compensate for motion as an image is acquired, but these techniques often require additional scanner-compatible equipment and can only be utilized during the scan. Additional processing is needed to remove motion from an image after the scan is acquired.

Though patient motion is a problem across the entire medical imaging domain, we focus specifically on resting state functional magnetic resonance imaging (rs-fMRI). rs-fMRIs measure the blood oxygen level dependent signal in an organ or organ system. Areas of an organ with greater activity require more oxygen than less active areas. When used to examine the brain, the signals recorded by the rs-fMRI are used as an effective approximation of the amount of activity occurring in different areas of the brain. The term "resting state" means that the patient is not performing any particular task, so any activity that occurs is from

underlying networks connecting different areas of the brain.

To gather enough data to fully evaluate these networks, a series of image volumes must be acquired over a period of several minutes. In a standard rs-fMRI, one new image volume is obtained approximately once every two to three seconds. To gather high quality data on such a short timescale, the rs-fMRI suffers from two major limitations: rs-fMR images have low physical resolution and are highly susceptible to motion. The first limitation can be addressed by obtaining an MR image with high physical resolution and registering the rs-fMRI to this structural image, but the second limitation is a significant problem. Patients undergoing a rs-fMRI scan are instructed to remain as still as possible for the entire duration of the scan, but this task is particularly difficult for populations of certain ages as well as populations who suffer from neurocognitive disorders. As a result, many rs-fMRI studies struggle to obtain enough low-motion scans to come to statistically significant conclusions. Although rs-fMRIs have great promise in the clinical domain, their usage is limited until the problem of patient motion is resolved.

As discussed above, behavioral and educational techniques have been developed to help the patient remain calm before and during the scan but do not prevent the patient from moving during the scan. Sedation or intra-scan motion monitoring approaches are difficult to integrate with MR scanners due to the constraints of MR safety requirements. Many methods have been developed to mitigate the effects of motion after the rs-fMRI is acquired. While different post-acquisition motion correction pipelines utilize different processing techniques, they begin with global volume registration. Global volume registration is the process used to align all volumes in a rs-fMRI sequence into the same physical space. Traditionally, all volumes in the sequence are registered directly to one volume. This approach can be effective in images where the subject remains relatively still throughout the duration of the scan, but is not as successful in images containing high quantities of patient movement.

We have developed an alternative volume registration framework which takes into account the spatiotemporal relationships between sequential volumes in the rs-fMRI sequence and uses these relationships during the registration process. Herein, we evaluate it further in the context of a complete motion correction pipeline across healthy and disease populations at various stages of life. In addition to reducing the effects of patient motion on image quality,

we are also interested in the patient motion itself. We believe there are relationships between different motion patterns, patient age, and clinical outcomes, and we have explored these relationships throughout our experiments.

The disease population we used for our study is a population with a variety of congenital heart defects. Congenital heart defects (CHDs) have many presentations, and all cause problems in a patient's heart structure and the structure of the surrounding vessels. It has been found that the development of cardiac problems *in utero* is often linked to delays in patient neurodevelopment. Research in the area of CHD and neurodevelopment has often focused on younger populations. However, treatment of CHDs has evolved over the past fifty years with the result that many CHD patients live to adulthood: every year, approximately 1.35 million children are born with a congenital heart defect and it is currently estimated that about 12 to 34 million adults are living with CHD [van der Linde et al., 2011]. Researchers have recognized the burden of neurocognitive disorders on the aging CHD population and are now starting to investigate the relationships between CHD and neurocognitive outcomes.

The process for objectively identifying neurocognitive disorders is still under development. Psychologists have developed and validated surveys to estimate a patient's neurocognitive status. These surveys vary with the child's. Initially, a parent fills out the survey on behalf of his infant or toddler child. When the child has reached certain developmental milestones, the parent and child might both fill out different portions of a different survey. At some point, the child can fill out his own survey. Psychologists may meet with the patient and his parents to determine a diagnosis. These survey based methods are highly subjective, and objective methods based on rs-fMRIs are being explored.

Eventually, clinicians will be able to develop a lifespan approach to managing CHD and neurocognitive disorders. As a community, we are still in the data-gathering stage of this research. We cannot afford to lose rs-fMRI scans of healthy or CHD patients in any stage of life because of motion. For these reasons, a cohort of healthy and CHD patient images are an ideal data set for our motion correction work.

The remainder of this document is laid out as follows. We elaborate on resting-state functional magnetic resonance images (rs-fMRIs) and their use for investigating functional brain networks in Chapter 2. In Chapter 3, we discuss congenital heart disease, its rela-

tionship with neurological conditions, and methods for evaluating neurological conditions. **??** transitions into methods for analyzing MRIs, machine learning techniques, and our approach to statistical analysis. We discuss our data for each cohort in Chapter 6, and explain the experiments we plan to do in **??**. Chapters 7 and 8 contain preliminary results and a discussion of these results from our initial study comparing two registration techniques in a neonatal data set.

2.0 RS-FMRIS AND PATIENT MOTION

This chapter discusses rs-fMRIs and how they are affected by patient motion. Specific topics include the structure of rs-fMRIs, sources of motion, current methods for preventing and managing motion in rs-fMRIs, quantifying motion, and usability criteria for using images corrupted by motion.

2.1 STRUCTURE OF AN RS-FMRI

A rs-fMRI scan produces a four dimensional image series. The first three dimensions are length, width, and depth and encompass the physical space occupied by the patient's head. The information in these three dimensions is interpreted as a three dimensional, volumetric image. The fourth dimension is time. The temporal dimension interacts with the spatial dimensions such that the contents of that image volume change with time. This concept of a 4D image can be illustrated in two different ways. The first is an ordered list of 3D image volumes. The second is a single 3D image volume where the value of each voxel is a temporal signal.

rs-fMRIs are discrete representations of continuous data. A new image volume of the patient's brain is acquired every two to three seconds. The image volume is composed of a three dimensional version of a pixel called a voxel (volume element). Just as the "distance" between each image volume encompasses a certain amount of time, each voxel encompasses a small volume of physical space. The transformations between the continuous physical and temporal dimensions and the discrete physical and temporal dimensions are the spatial and temporal resolutions.

Figure 1: The patient's brain activity effectively passes through several filters before an MRI scanner produces a visually interpretable image sequence.

An rs-fMRI is considered to have relatively low spatial resolution but high temporal resolution. The physical size of a single voxel seems small at about 4 mm^3, but this resolution is not granular enough to capture details about activity within small structures of the brain. The activity information recorded during a rs-fMRI must be combined with the detailed anatomic information from a structural MRI to know precisely which areas of the brain are active at each point in time. A structural MRI volume takes much longer to acquire than a rs-fMRI volume, which can be obtained every two to three seconds. Unfortunately, the patient's position and neural activity can change faster than the image volume can be acquired. As a result, a temporal resolution of two to three seconds is not fast enough to actively compensate for sources of noise which confound the BOLD signal.

2.2 CONFOUNDS IN RS-FMRIS

The BOLD signal present inside a patient's brain is not recorded with complete accuracy by an MRI scanner. Even if the same patient exhibited the exact same BOLD signal during two different scans, the recorded image sequences would vary slightly. There are a number of confounds that impact the image sequence viewed by a radiologist, and we give an overview

of them in Figure 1.

The first filter in Figure 1 is the patient's physiology. A rs-fMRI is not sensitive enough to detect brain activity on a neuronal level. Instead, it measures the changes in the amounts of deoxygenated hemoglobin in the brain. The deoxygenated hemoglobin quantities are highly correlated with brain activity because active areas of the brain use more oxygen than inactive areas, but this BOLD signal is still only an approximation of brain activity.

The second filter in Figure 1 is changes to the signal that occur due to patient motion. During every medical imaging scan, the patient will naturally perform small, automatic movements due to regular bodily functions. Minuscule movements caused by cardiac activity may disrupt scans with high spatial resolution or with high sensitivity to the movement of blood molecules. Larger movements caused by respiration result in motion artifacts in images of the thoracic and abdominal cavities.

Other motions occur on a larger and more conscious scale. It is important to note that different populations may exhibit more of certain macro-motions than others. The patient may fidget or shift his gaze when he becomes bored in the scanner. If the patient falls asleep during a scan, there may be slight movement as the body relaxes and retenses if the patient wakes. Certain MRI protocols are known to produce loud sounds: during one of these protocols, the patient may become surprised and react by jumping. Additionally, clausterphobic patients or patients who feel secure around specific people that are not allowed in the scanner room may become agitated.

Both the small-scale, automatic motions and the large-scale, reflexive motions corrupt the BOLD signal. These effects of patient motion will be discussed in depth in the next section.

The third filter in Figure 1 is the unique properties of the scanner. The acquired image sequence will vary slightly even in machines made by the same company because each scanner has a unique primary magnetic field, B0. The B0 inhomogeneities can be measured using a primary field map. These field maps can be used to correct signals displaced by the B0 field, though they cannot be used to recover signals corrupted by the field.

The final filter is also related to the properties of the MRI scanner. The image sequence produced by a scanner is dependent on the scanner vendor. Different vendors use different

proprietary algorithms to convert the signal recorded by the scanner in k-space into a visually interpretable image sequence. Between the B0 inhomogeneities and the scanner vendor differences, the differences in the scanners used to acquire the sequences must be resolved before images from different scanners can be compared.

2.3 EFFECTS OF PATIENT MOTION

In general, motion affects an acquired image sequence in three ways. The first and most obvious effect is the position of the patient changes throughout the sequence. The second effect is due to the way changes in the patient's position affect the signal recorded by the scanner. The third effect is due to the magnetic fields in patient tissue and changes in their orientation within B0. These three effects will hereafter be referred to as the positional effect, the spin history effect, and the susceptibility effect of motion.

Due to their low spatial and high temporal resolutions, rs-fMRIs are highly susceptible to all types of motion outlined in the previous section. The effects of motion on rs-fMRIs can be clearly divided into two categories: the effect on patient position and the effect on the recorded BOLD signal.

2.3.1 The Positional Effects of Motion

The technique used for analyzing rs-fMRIs, called functional connectivity analysis, assumes that the contents of one voxel at every time point during the sequence all contain signal from a single point in the brain. This assumption is vital in the process of inferring networks of neuronal activity.

While rs-fMRIs have a spatial resolution on the order of millimeters, neuronal activity occurs on the spatial resolution of microns. As a result, each voxel in a rs-fMRI volume contains information from a number of neurons. The smallest movement of the patient can alter the voxel to which a cluster of neurons contributes. These seemingly insignificant changes can alter the position of the patient enough to cause the voxels to record signals

from different brain regions or even tissue types. This change in voxel location within the brain violates the assumption of voxels recording from the same location within the brain for the duration of the sequence.

2.3.2 The Spin History Effects of Motion

In addition to changing the recorded position of the subject, motion impacts the established spin gradients, which introduces artifacts into the image sequence.

During an ideal MRI scan, the patient is sitting in the scanner and all molecules are aligned with the primary magnetic field B_0 in a relaxed state. Then, a radiofrequency (RF) pulse is applied to the field. The purpose of the pulse is to excite the molecules in a certain volume of physical space to orient the molecules to align to a secondary field in a different plane. When the pulse ends, the molecules precess back to their orientation in B_0. As they do, their small magnetic fields induce electric currents on the RF coil. The currents are received by the scanner as signals in frequency space. The volume of the space intended to be excited is known, and the signal produced by the induced electric current is used in conjunction to reconstruct the image in voxel space.

However, when the patient moves, the volume of space which was thought to be excited is not actually excited: some other volume of space, which may or may not overlap with the intended volume of space, is excited instead. Because the MRI scanner has no way to know this assumption is not true, it does not know that not all of the molecules in its intended area are relaxed and correctly aligned to the B_0 field at the end of the RF pulse. The scanner proceeds with the next RF pulse, which excites a new set of "relaxed molecules", some of which are still excited from the previous pulse. As a result, the signals produced in the second RF pulse are different than they should be. For example, signals that are smaller than they should be result in dark shadows within motion affected volumes of the sequence.

The previous few paragraphs in this section describe how motion disrupts the magnetic spin gradients present in the patient during an rs-fMRI scan. The spin gradients need time to recover to the correct magnetic field orientation, and up to eight to ten seconds may pass before the recovery is complete [Power et al., 2014]. While the spin gradients

are reorienting, the recorded BOLD signal will vary more than usual between temporally neighboring volumes. These variations are more difficult to quantify than the positional effects of motion.

2.3.3 The Susceptibility Effects of Motion

The susceptibility of a material describes how the material will behave when placed in a magnetic field. Most materials are either paramagnetic or diamagnetic. Paramagnetic materials are attracted to and align with magnetic fields while diamagnetic are repelled from and become anti-aligned with magnetic fields. Additionally, paramagnetic materials contribute to the magnetic field where they interact with it while diamagnetic materials detract from it.

2.4 MEASURING MOTION

Even though we described three effects of motion on rs-fMRIs in the previous section, these effects impact the sequence in two areas: the position of the patient and spurious signal correlations throughout the sequence.

2.4.1 Measuring Motion: Patient Position

The effect of motion on patient position is measured in terms of the difference in the positions of the contents of temporally neighboring image volumes. The difference in position is determined using metrics calculated by performing rigid volume registration on the two volumes. In rigid volume registration, one volume is chosen as the reference volume and the other is considered the moving volume. The reference volume remains stationary while the moving volume is translated and rotated in three-dimensional space on top of it. The registration is considered complete when the position of the patient in the moving volume matches the position in the reference volume.

The moving volume can undergo linear or nonlinear transformations. Linear transformations include translation, rotation, and affine transformations along all three spatial dimensions as well as a scaling transformation. These transformations move the image volume as a whole: all voxels in the moving image remain in the same location relative to their neighbors. On the other hand, nonlinear transformations have the ability to warp the contents of the moving volume so that it better matches the contents of the reference volume. Nonlinear transformations are more complex than linear transformation. They involve additional image processing steps such as smoothing and voxel interpolation.

Even in cases when nonlinear transformations are used, the registration process begins with the translation and rotation transformations. The three translation and three rotation parameters used to achieve the best alignment are used to calculate the positional change between the image volumes. The positional change between temporally neighboring volumes is called the framewise displacement (FD).

Several researchers have proposed slightly different methods for calculating the FD. Power et al., Jenkinson et al., and Dosenbach et al. each propose a slightly different method for calculating the FD [Power et al., 2012] [Jenkinson et al., 2002] [Dosenbach et al., 2017]. All three FD calculations produce correlated metrics: the FD metric proposed by Power et al. produces measurements approximately twice as large as the metric proposed by Jenkinson et al., and Dosenbach et al. reported a high correlation between their FD and Powers FD [Yan et al., 2013b] [Dosenbach et al., 2017]. Herein, we use Power et al.'s version of the FD metric.

2.4.2 Measuring Motion: Spurious Signal Correlations

Both the spin history and susceptibility effects of motion contribute to alterations in the signal recorded and reconstructed by the MRI scanner. Without B0 field maps and susceptibility maps, it is difficult to separate the impact of each of these factors on the recorded signal. We assume at this point that both the spin history and the susceptibility effects contribute equally to changes in the recorded signal intensity.

One popular metric to measure changes in the recorded signal due to patient motion

was developed by Smyser et al. in 2010. Their metric is called DVARS, which measures the temporal **d**erivative of the root mean squared **var**iance over the voxels between two volumes [Smyser et al., 2010]. Power et al. explain the steps to calculate DVARS in a separate study [Power et al., 2012]. The DVARS value is calculated in two steps. The first step uses backward differences to approximate the derivative of the BOLD signal change between volumes J_i and J_{i-1} at every point $\vec{x}$ contained in both image volumes:

$$\frac{\partial}{\partial t} J_i(\vec{x}) \approx J_i(\vec{x}) - J_{i-1}(\vec{x}). \tag{2.1}$$

The second step calculates the root mean square of the approximated derivatives for all N points $\vec{x}$:

$$DVARS(J_i) = \sqrt{\frac{1}{N} \sum_{\vec{x} \in J_i, J_{i-1}} \left(\frac{\partial}{\partial t} J_i(\vec{x}) \right)^2}. \tag{2.2}$$

DVARs measures the change in BOLD signal intensity, which is highly related to motion-induced spin gradient changes.

2.5 MOTION PREVENTION

Various techniques and protocols have been developed to prevent patients from moving during the image acquisition process. Not all of these techniques are suitable for all patient populations, and some techniques have been designed specifically for certain populations.

2.5.1 Pre-Scan: Education

Educational material can be used to help the patient understand what to expect during an MRI scan as well as to teach the patient different behavioral coping strategies. The education materials can be used either before or upon arrival at the imaging facility. Most of the formal literature focuses on informative, distraction, and behavioral techniques to use during pediatric MRI scans, though many of the following approaches could be adapted for use with adults.

In a review of the available literature, Alexander found several commonly used techniques to educate pediatric patients before and comfort or distract pediatric patients during radiology procedures [Alexander, 2012]. Tools such as educational coloring books and short videos can expose patients to the types of equipment they can expect to see using a familiar, engaging medium. Pediatric patients can learn coping strategies to employ during the scan such as breathing techniques, imagery, and positive statements. Alexander notes that allowing a pediatric patient to choose a behavioral coping strategy gives the patient a sense of control and may encourage the patient to cooperate during the MRI acquisition.

Mock scanners and MRI simulators can also help the patient feel more comfortable during the scan. Barnea-Goraly et al. showed that both a commerical MRI simulator and a low-tech mock scanner desensitized pediatric patients between four and ten years of age to the MRI scanner with the results that 92.3% of the acquired images could be used in high-resolution anatomical studies [Barnea-Goraly et al., 2014].

Several groups have investigated the role of auditory and visual distraction during an MRI acquisition. Headphones with music and stories or MR compatible video goggles can distract patients from the tedium of the scan [Alexander, 2012] [Barnea-Goraly et al., 2014] [Harned and Strain, 2001]. Khan et al. found that a relatively simple moving light show can be helpful in distracting younger patients [Khan et al., 2007]. Garcia-Palacios et al. performed a case study comparing the efficacy of music and immersive virtual reality tools as distractions during a mock scan [Garcia-Palacios et al., 2007]. They suggest that immersive virtual reality may help decrease patient anxiety during a scan more effectively than music alone. As virtual reality technology improves, it may join headphones and MR compatible video goggles as an available distraction method.

Another helpful source of distraction for pediatric patients could be the patient's parent or parents. Having a parent involved with the scanning process may calm the patient and encourage him to cooperate; however, parental distress can further upset an anxious patient and complicate the scanning process [Alexander, 2012].

These techniques for educating the patient and helping the patient cope with the anxiety that can accompany an MRI scan all depend on the ability of the patient to understand instructions and communicate with the scan team. Due to the gap in communication abilities,

these techniques are not useful for young patients such as neonates, infants, toddlers, and possibly elementary school aged children. Other patient populations, such as those with developmental delays and neurobehavioral disorders, may also have difficulty adhering to these protocols. Even in patients with developed and intact communication skills, the techniques outlined here do not actively prevent the patient from moving during the scan: they only help the patient feel more comfortable with the MRI environment.

2.5.2 During Scan: Sedation

Sedation can be used to help a patient tolerate an MRI scan. Murphy and Brunberg retrospectively analyzed seven weeks of data from the MR department and found that 14.2% of their adult patients required some form of sedation [Murphy and Brunberg, 1997]. In a study about claustrophobia and MR acquisitions, Dewey et al. report that out of 55,734 patients who underwent MRI scans, a total of 1004 patients experienced claustrophobia and 610 of these patients required intravenous sedation before their scans [Dewey et al., 2007]. Even though sedation allowed the patients mentioned in this paragraph to undergo an MRI scan, the authors of both studies note that sedation can result in adverse events and advise the reader to avoid patient sedation if possible.

Sedation can be used with pediatric patients, though the risks are more significant than with adult patients. Studies have shown that sedation for pediatric imaging can lead to hypoxemia and inappropriate sedation levels during image acquisition [Malviya et al., 2000]. Pediatric patients can also expect "motor imbalance and gastrointestinal effects," as well as agitation and restlessness for a period of hours after waking from sedation.

A report from the American Academy of Pediatrics and the American Academy of Pediatric Dentistry outlines the minimum set of criteria needed for a pediatric patient to be sedated for a procedure [Coté and Wilson, 2016]:

- The patient must be a suitable candidate for sedation based on their medical history and medical needs.
- The patient's health status must be evaluated and verified by the sedation team prior to the procedure.

- Informed consent must be obtained prior to the procedure.
- Instructions for what to expect and how to transport the patient home safely must be provided to the patient's responsible adult.
- At least one responsible adult must be with the patient at the medical facility, though the report recommends that two adults are present for patients who travel to and from the facility using car seats. This practice ensures that one adult can monitor the patient after the procedure while the other adult drives.
- The patient's food and drink intake prior to the procedure should be taken into account to minimize the risk of pulmonary aspiration.
- The clinician administering the sedation must have immediate access to emergency facilities, personnel, and equipment, and should monitor the patient for adverse events including respiratory events, seizures, vomiting, and allergic reactions.
- There must be a clear protocol outlined for immediately accessing these emergency services.
- Emergency equipment and drugs appropriate for the patient's size and age must be immediately available in case the patient needs to be resuscitated.
- The information about the procedure must be correctly documented.
- The facility should have a dedicated recovery area, and the status of the patient should be recorded when he is discharged. The patient should not be discharged if his level of consciousness and oxygen saturation do not meet recognized guidelines.
- The patient may be held at the facility for prolonged monitoring after the procedure.

This report clearly states that the levels of monitoring suggested above should serve as minimum levels of involvement: clinicians should increase patient monitoring as needed for complex cases. Rutman has a similar and detailed perspective on patient monitoring during and after sedation, adding that two independent medical personnel should be present during the scan and one should be present until the patient is discharged [Rutman, 2009]. Rutman also notes that all sedation and monitoring equipment must be MR compatible, which is a simple but important safety constraint. This constraint makes sedation less advisable if the appropriate equipment is not available.

Sedation in neonatal and infant populations is not recommended. The U. S. Food and Drug Administration (FDA) issued a warning in late 2016 about repeated use of sedation or general anesthesia for patients under three years of age or for pregnant women during their third trimester [United States Food and Drug Administration, 2016]. The warning states that while a single, relatively short exposure to sedative and anesthetic drugs is unlikely to impact the patient, the effects of prolonged exposure to these drugs are still being studied. Studies of sedative and anesthetic drugs in multiple animal models have shown that these drugs can lead to loss of nerve cells in the brain when the animals undergo prolonged, repeated exposure to them during period of brain development. More data is needed to determine if this effect translates to humans.

2.5.3 During Scan: Feed and Sleep Protocols

Neither sedation nor educational and behavioral techniques are appropriate to use with neonatal patients, but rs-fMRIs in neonates and infants are invaluable in studying early brain development and neurological diseases [Smyser and Neil, 2015]. A set of protocols have been developed specifically for scanning neonates without sedation. These protocols are referred to as "feed and sleep" or "feed and bundle" protocols.

Windram et al. describe a protocol in which the infant is deprived of food for four hours prior to the scan [Windram et al., 2011]. At the scanning facility, the patient is fed by his mother, swaddled, and placed in a vacuum-bag immobilizer for the duration of the scan.

Rather than deprive the patient of food prior to the scan, Gale et al.'s protocol recommends timing the scan so that the patient is fed after arrival on site and less than 45 minutes before the scan [Gale et al., 2013]. The patient's ears are protected from the noise of the MR scanner by a layer of dental putty followed by headphones, and held in place by a hat. The patient is the swaddled and placed in the scanner once he is asleep. Additional foam padding is used to cushion the patient's head and provides extra noise protection.

Mathur et al. describe a protocol similar to the previous two: the patient's feeding schedule is adjusted so that he feeds 30-45 minutes before the scan time, and he is swaddled, given ear protection, and placed in a vacuum-bag immobilizer [Mathur et al., 2008].

When performed correctly, these protocols are generally successful and the neonatal patient will sleep for the duration of the MRI scan. However, the patient may shift slightly while asleep or may wake up and move mid-scan.

2.6 PROSPECTIVE MOTION CORRECTION

Since motion cannot be completely eliminated from rs-fMRI scans, different approaches have developed for correcting for the effects of motion after the scan. These approaches can be divided into two groups: those which monitor the patient's motion during the scan and those which work solely on the acquired sequences.

2.6.1 Optical Motion Correction

Several groups have developed methods for actively accounting for changes in the patient's position during an MRI scan. Optical-based methods record the patient's position using a combination of markers placed on the patient and one or more MR compatible optical cameras placed the scanner bore. The changes in the patient position from one time point to the next are used to update the MR parameters in real-time. Real-time updates of the MR parameters result in decreased spatial and spin-history effects of motion in the acquired sequences.

The first report of successful prospective motion correction using optical cameras and markers was by Zaitsev et al. in 2006 [Zaitsev et al., 2006]. Their dual camera system was located outside of the MRI scanner and focused on the patient inside the system. Four reflective markers were attached to a modified mouthpiece originally designed for patient immobilization. Changes in the translation and rotation of the patient were recorded and processed during the exam. The processed changes were sent in real-time to the MRI scanner which used them to update the gradient orientations, RF frequencies, and RF phases at every time point during the acquisition process.

Aksoy et al. simplify this approach by using a single in-bore optical camera and replacing

the 3D markers with a small 2D chessboard grid [Aksoy et al., 2008]. Properties intrinsic to the camera as well as information about the camera's placement within the MRI scanner were recorded prior as part of a calibration process. During the scan, patient movements recorded using the optical camera were used to calculate the relationship between the patient's position at the current time point in the physical space and the patient's position at the initial time point in the MR space. The transformation needed to translate between these two positions was calculated on a laptop and passed to the MRI scanner to correct for motion in real-time. The camera used to record the position of the chessboard is mounted on the head coil. If the patient moves his head significantly, the camera will only be able to record the position of part of the chessboard marker. This limitation makes it difficult for the computer vision processing to identify the independent features on the standard chessboard.

Forman et al. modified the chessboard marker to improve its flexibility [Forman et al., 2011]. To differentiate between the different blocks in the chessboard, they added a unique, machine readable symbol to each black block in the chessboard. The symbols were chosen to be unique even in the event of rotation so that the identification of each block would be robust to rotation movements. The chessboard marker was embedded with MR-detectable agar so that the position of the marker could be detected in the MRI scan as well as by the in-bore camera. At each point during the scan, the image recorded by the in-bore camera was sent to a computer independent from the MRI controller. The independent computer detected the blocks of the chessboard and identified their spatial locations using the symbols contained within them. Their positions were checked by confirming the locations of the symbols with respect to each other. The confirmed locations of the corners of the black boxes were used to estimate the position of the patient, which was then sent to the MRI controller so that the magnetic gradients and RF hardware could be updated for the time point. The authors note that the latency of the system is a significant limitation to their system, but overall they experienced an increase in the accuracy of the estimates of the patient's position.

Several companies have developed commercial products for prospective motion correction in neurological images. KintetiCor's system uses a high resolution camera and a physical marker to detect motion [KinetiCor Biometric Intelligence, 2019]. The camera's resolution allows it to detect respiratory and cardiac motion through changes in skin displacement on

the patient's forehead. The physical marker consists of pair of rectangles containing several concentric circles which are connected via a bridge across the nose. Any patient movement is reflected in the movement of the markers, which is also tracked through the camera. Both the camera system and the marker are MR compatible. Another company, TracInnovations, uses a stereo camera system to track all patient motion [TracInnovations, 2019]. At the start of the scan, the stereo camera obtains a point cloud of the patient's position at that time. The points in the point cloud are averaged together to create a primary marker. Small facial motions, cardiac motion, and respiratory motion, are monitored using the point cloud. Larger head motions are monitored using both the point cloud and the primary marker. These two systems both allow prospective motion correction to be turned on or off: if the prospective motion correction is off, the system will still acquire the motion parameters so that the motion can be corrected retrospectively.

The methods discussed above have a few limitations due to the optical camera setups. For precise real-time motion correction, the camera or cameras must be carefully placed so that the position of the marker on the patient can be recorded. They must have a clear line of sight, which means they will be in the same room as the MRI scanner, if not within the scanner bore. The cameras and markers must be MR compatible, and the positions of the cameras and markers in physical space relative to the visual markers on the patient must be known. These positions are vital for the calculations used to measure the motions. Even if the motion measurements are accurate, the changes in position that are recorded and used to adapt the scan parameters will only be true for rigid body motion of the body part to which the markers are attached: any distortion of soft tissue will not be accurately accounted for during the motion correction unless the camera system was specifically built for and trained to do so.

2.6.2 External Sensors

Cameras are not the only type of external sensor that can be used to measure motion during a rs-fMRI scan.

There is a class of sensors which can take advantage of electrophysics properties of an

MRI scanner. These sensors include wired nuclear magnetic resonance field probes, wireless inductivity coupled markers, and off-resonance markers. The fact that these sensors directly interact with the magnetic field of the MR scanner means that protocols using these sensors must be modified to account for them. As a result of the protocol modification, the scan time might need to be extended.

As mentioned earlier in this chapter, respiration is a source of patient motion. Since respiration is relatively periodic, it can be monitored and accounted for within a scan protocol via gating. Gating prevents an image from being acquired unless the patient is in the expected state. In the case of respiration, the expected state is either complete inhalation or exhalation. The state of a patient's respiration can be tracked using respiration bellows. After acquiring the MRI sequence, volumes in the sequence can be grouped depending on when they were recorded in the breathing cycle. By only using volumes recorded during the same stage of the breathing cycle, the effects of respiratory motion can be mitigated.

Ultimately, the addition of extra sensors complicate the process and set up of a rs-fMRI scan.

2.6.3 Image Signal Motion Monitoring

Dosenbach et al. have developed a tool to evaluate motion in rs-fMRI sequences as they are acquired [Dosenbach et al., 2017]. It registers each volume to the initial volume of the rs-fMRI sequence immediately after the new volume is recorded. The parameters produced by this registration are used to calculate the framewise displacement between pairs of volumes, which is then compared to a set of displacement thresholds associated with the scan quality. The number of volumes that meet each threshold is used to determine how many more volumes are needed to obtain five minutes of low-motion volumes. This method for assessing the quality of a scan in real time is useful for ensuring images are acquired with a sufficient number of low-motion volumes. It can also aid the technologists in determining whether to prematurely terminate a scan, which may be desirable if the amount of time needed to obtain enough low-motion volumes is greater than the amount of time remaining for the patient in the scanner.

2.6.4 General Limitations of Prospective Motion Correction

All types of prospective motion correction introduce a delay into the scanning process. The delay is due to the additional processing of some metrics to determine the patient's position, the transmission of these metrics to the MR scanner, and the adjustments the scanner makes to its next set of measurements. These alterations to the image acquisition during prospective motion correction actively change the image as it is acquired. Maclaren et al. note that while prospective motion correction reduces imhomogeneities in the B_0 field, the B_0 field will still change when the patient moves and may change while the motion correction is occuring [Maclaren et al., 2013].

In order to view a scan not impacted by prospective motion correction, the patient often must undergo a second scan. It may be wise to build the second image acquisition into the same scan period as the prospectively motion corrected scan: unsuccessful prospective motion correction has the potential to drastically corrupt the acquired scan [Zaitsev et al., 2017].

Finally, though prospective motion correction has great power for managing motion during a scan, it cannot be used to recover motion-corrupted data in existing data sets.

2.7 RETROSPECTIVE MOTION CORRECTION

Many groups have put significant effort into developing techniques for motion correction after the scan is acquired. Here, we discuss several commonly used techniques: volume registration, denoising, and filtering.

2.7.1 Volume Registration

The rs-fMR image is stored in computer memory as a set of 3D matrices. The values in corresponding cells of each matrix are considered to be aligned in this digital space (voxel space). The voxel space is defined by the imaging protocol and relates to the physical space through the spatial resolution of the image. Even though the spatial and voxel spaces

for the image align, the contents of the image volumes may be misaligned due to patient movement. Because we cannot assume that an image is completely motion-free, we cannot directly compare the contents of each image volume in the rs-fMRI sequence. However, we can use image registration to align the contents of the image volumes to reduce the impact of motion on patient position.

Image registration is the process of morphing the contents of one image so that they overlap optimally with another image. The morphing operations include translation, rotation, scaling, skewing, and nonlinear adjustments. The linear and affine operations in this list should be used to perform rigid body registrations for organs such as the brain. Nonlinear operations can be used to fine-tune the alignment of more pliable organs such as the liver. All morphing operations are applied to one image repeatedly until it's contents optimally match those of the static reference image as determined by a chosen similarity metric.

One of the earliest examples of image registration was described by Friston et al. in 1995 [Friston et al., 1995]. They performed image registration on positron emission tomography (PET) scans and MRI scans of a human brain. During the registration process, one scan was designated as the "reference" image, which remained stationary, and the other scan was designated as the "object" image, which was transformed to match the reference image. Constraining the alignment process to transforming a single image into the coordinates of the other image rather than transforming both images into an independent coordinate frame simplifies the registration process.

When performing image registration on a sequence of image volumes, one volume must be chosen as the reference volume for the entire sequence. All other volumes in the sequence are registered to this volume. An example of this process can be seen in Figure 2. In subsequent work, Friston et al. used the first volume in the rs-fMRI sequence as the universal reference image [Friston et al., 1996]. Common choices for the reference volume include the volume with the least FD to all other volumes in the sequence, a volume produced by averaging all volumes in the sequence, or the first volume in the sequence [Friston et al., 1996] [Liao et al., 2005]. In our implementation, we chose to use the first volume in the sequence as the reference volume.

One drawback to this traditional approach to volume registration is that it only minimizes

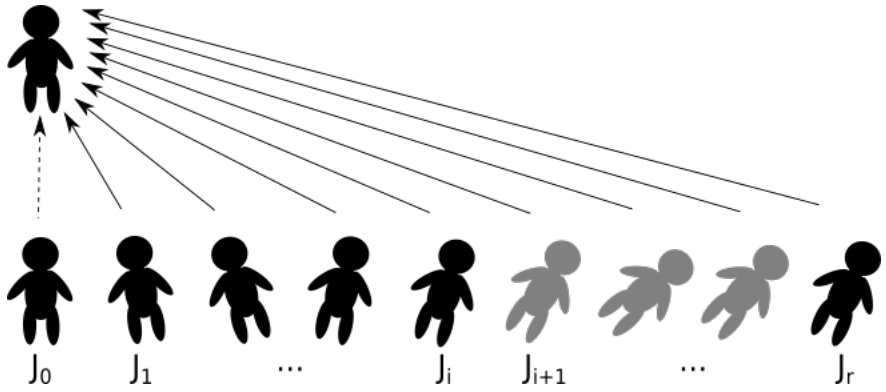

Figure 2: The traditional approach to volume registration in an rs-fMRI sequence consists of registering all volumes in the sequence to a single reference volume.

the differences between all the image volumes in the sequence and the reference volume. The key word here is minimizes: minimizing differences between image volumes does not mean that there are no differences between the image volumes. Image registration is an optimization problem, and its goal is to find the overlap between a pair of volumes with as few differences as possible either within a defined time period or until the optimization cost does not change above a certain tolerance for a certain amount of time. These practical constraints on optimization problems mean that there may still be differences between other pairs of image volumes in the sequence that do not include the reference volume.

Variations on Friston et al.'s framework have been developed over the last two decades. Liao et al. suggested that a rs-fMRI sequence could be viewed as a hidden Markov model, and reflected this idea in their suggested registration framework [Liao et al., 2016]. They still use the first volume in the image sequence as the reference volume. Their framework uses the transformation of the previous volume to the reference volume to initialize the transformation for the current volume and the reference volume.

It has been demonstrated that image registration across the entire image sequence reduces the effects of motion on the image sequence, though they do note that motion also effects the image due to changes in the spin history of the image. These effects are not correctable by global volume registration alone and will be discussed later in this chapter.

2.7.2 Denoising

Denoising techniques can be applied to a rs-fMRI after global volume registration is completed. They consist of regressions of various confound variables.

Regression of the global signal (global signal regression, GSR) corrects for variance between temporal signals within a voxel and for the mean BOLD signal across all voxels [Power et al., 2014] [Satterthwaite et al., 2013] [Yan et al., 2013a] [Yan et al., 2013b]. GSR has been shown to reduce spuriously increased long-distance correlations in functional connectivity studies, but may inadvertently weaken shorter-distance connections [Jo et al., 2013] [Power et al., 2014] [Satterthwaite et al., 2012].

Other regression parameters have been investigated. Commonly, the six rigid realignment parameters and their first order derivatives are suggested as regression parameters [Power et al., 2012] [Satterthwaite et al., 2012] [van Dijk et al., 2012]. More recently, researchers have also incorporated the rigid realignment parameters from surrounding timpoints [Power et al., 2014] [Satterthwaite et al., 2013] [Yan et al., 2013b].

, signals from white matter or cerebral spinal fluid [Power et al., 2014] [Satterthwaite et al., 2013] [Yan et al., 2013b] [Jo et al., 2010], and components identified using principal or independent component analysis [Pruim et al., 2015] [Salimi-Khorshidi et al., 2014] [Behzadi et al., 2007]. Regression of each of these sets of parameters has been shown to reduce the effects of motion in the sequence but not remove them entirely [Power et al., 2015] [Parkes et al., 2017].

Patriat et al. performed a robust comparison of different regression parameters on their MotSim motion data set [Patriat et al., 2017]. They included rigid realignment parameters, but also used parameters obtained by performing principle component analysis (PCA) on the image sequences. PCA generates a set of linear, uncorrelated components that reflect the main features of a patient's motion. The list of parameter combinations included

- 12mot: The six rigid realignment parameters and their first derivatives,
- 12for: The first 12 principal components of the whole brain before realignment,
- 12back: The first 12 principal components of the whole brain after realignment,
- 12both: The first 12 principal components of the whole brain both before and after realignment,

- 24mot: the six rigid realignment parameters of the current volume, the six rigid realignment parameters of the previous volume, and the square of these rigid realignment parameters,
- 24both: the first 24 principle components of the whole brain before and after realignment.

They found that the features extracted from the image sequence using PCA explained more variance in the image sequence (measured using R^2) than the rigid realignment parameters. They showed that increasing the number of regressors increased the amount of variance explained, but with diminishing returns. While their work is promising, their experiment was performed on a simulated data set using healthy subject data and required an accurate estimate of the subject's head motion.

2.7.3 Filtering

Filtering, which is also referred to as censoring, involves the identification and removal or interpolation of volumes containing high quantities of motion. Two popular techniques are scrubbing and spike regression. Power et al.s scrubbing technique removes volumes with more than 0.2 mm of FD [Power et al., 2012]. Spike regression identifies volumes with large FD and replaces them with interpolated volumes [Satterthwaite et al., 2013]. Unfortunately, these filtering techniques ultimately result in the loss of data as volumes are removed from the sequence. A third technique called despiking detects signal spikes at the voxel level and interpolates over the spikes [Jo et al., 2013] [Patel et al., 2014]. Despiking does not remove volumes, but could accidentally remove valuable signals.

2.7.4 Spin History Distortion Correction

A number of post-acquisition methods have been developed specifically to correct for distortions due to the impact of motion on the magnetic field. The usability of these dynamic distortion correction methods has been studied in a few specific cases, but their generalizability has yet to be confirmed in a broader range of fMRI studies [Zaitsev et al., 2017].

2.8 IMAGE USABILITY

Even though the effects of motion on the patient position and the recorded signal can be measured, we still need gold standard criteria to determine whether an image containing motion can be used. Patients move slightly due to breathing and cardiac function, and the BOLD signal naturally fluctuates over time. Some motion is expected; however, we need to know how much motion can be present in the image before it is considered to be corrupted by it. Power et al. established thresholds for FD and DVARS to determine the usability of a pair of images:

- FD less than or equal to 0.2 mm from previous volume, and
- DVARS less than or equal to 25 units on a normalized scale of [0, 1000] signal units [Power et al., 2014]

Image volumes that meet these criteria are considered to be low-motion.

The time span of low-motion data is highly debated. van Dijk et al. established that approximately five minutes of low-motion data is sufficient for use in functional connectivity analysis [van Dijk et al., 2012]. However, a recent study by Laumann et al. suggests that at least 10 minutes of low-motion data is essential for obtaining high-quality results [Laumann et al., 2015]. From a practical standpoint, it is difficult to obtain even five minutes of low motion data from certain patient populations, so radiology technicians and neuroimaging study designers are often content with the five minute time standard.

2.9 SUMMARY

Resting-state fMRIs are four dimensional images which record BOLD signal in active areas of the brain. The BOLD signal can be used to evaluate the functional connnectivity of different underlying networks in a patient's brain. Since rs-fMRIs are highly sensitive to motion, clinicians and psychologists have devised techniques to inform patients about what they can expect during an MRI scan as well as different coping mechanisms to help them

remain calm during the scan. These techniques do not prevent the patient from moving, but approaches that do are not always appropriate to use during a rs-fMRI scan. Techniques and algorithms to prospectively and retrospectively remove motion from rs-fMRIs have also been developed, though they are not always successful in removing the effects of motion. Ultimately, the amount of motion present in the rs-fMRI sequence dictates whether or not the sequence can be used in clinical or research applications.

In the next chapter, we will discuss rs-fMRIs in the context of our chosen population of CHD patients.

3.0 CLINICAL BACKGROUND

3.1 CONGENITAL HEART DEFECTS

Congenital heart defects and congenital heart disease (CHD) both refer to defects in the heart or the vessels around the heart which formed during fetal development. Heart defects affect how blood moves into, through, and away from the heart. CHD can affect any combination of heart chambers and blood vessels with varying degrees of severity. The lesions prevent the cardiopulmonary system as a whole from functioning correctly, but pinpointing and treating the defects effectively can be a complex process.

There are a number of genetic and environmental factors associated with different presentations of CHD [Mozaffarian et al., 2016]. Genetic conditions such as Down syndrome, Turner syndrome, 22q11 deletion syndrome, Williams syndrome, and Noonan syndrome are associated with different CHD presentations. Maternal behaviors such as smoking and binge drinking are known to cause heart problems in the fetus. Other maternal risk factors are obesity, folate deficiency, and living at a high altitude. Paternal exposure to phthalates, anesthesia, sympathomimetic medications, pesticides, and solvents may increase the risk of the fetus for developing CHD. While there are quite a few factors in this list, there are many CHD cases whose causes are unknown.

The process of diagnosing CHD can begin before birth. A specialized ultrasound test called fetal echocardiography can detect heart abnormalities as early as the second trimester of the pregnancy. Additional tests, such as amniocentesis and follow-up ultrasounds may be used to determine treatment options before the patient is born. Generally, severe CHD cases present and are detected at earlier stages, but minor defects may not become apparent until the patient is older. Tests used to diagnose CHD in postnatal patients include electro- and

Table 15-3. Estimated Prevalence of Congenital Cardiovascular Defects and Percent Distribution by Type, United States, 2002* (in Thousands)

	Prevalence, n			Percent of Total		
Type	Total	Children	Adults	Total	Children	Adults
Total	994	463	526	100	100	100
VSD†	199	93	106	20.1	20.1	20.1
ASD	187	78	109	18.8	16.8	20.6
Patent ductus arteriosus	144	58	86	14.2	12.4	16.3
Valvular pulmonic stenosis	134	58	76	13.5	12.6	14.4
Coarctation of aorta	76	31	44	7.6	6.8	8.4
Valvular aortic stenosis	54	25	28	5.4	5.5	5.2
TOF	61	32	28	6.1	7	5.4
AV septal defect	31	18	13	3.1	3.9	2.5
TGA	26	17	9	2.6	3.6	1.8
Hypoplastic right heart syndrome	22	12	10	2.2	2.5	1.9
Double-outlet right ventricle	9	9	0	0.9	1.9	0.1
Single ventricle	8	6	2	0.8	1.4	0.3
Anomalous pulmonary venous connection	9	5	3	0.9	1.2	0.6
Truncus arteriosus	9	6	2	0.7	1.3	0.5
HLHS	3	3	0	0.3	0.7	0
Other	22	12	10	2.1	2.6	1.9

Average of the low and high estimates, two thirds from low estimate.[24]ASD indicates atrial septal defect; AV, atrioventricular; HLHS, hypoplastic left heart syndrome; TGA, transposition of the great arteries; TOF, tetralogy of Fallot; and VSD, ventricular septal defect.

*Excludes an estimated 3 million bicuspid aortic valve prevalence (2 million in adults and 1 million in children).

†Small VSD, 117 000 (65 000 adults and 52 000 children); large VSD, 82 000 (41 000 adults and 41 000 children).

Source: Data derived from Hoffman et al.[24]

Figure 3: Table of prevalences of congenital heart defects borrowed temporarily from [Mozaffarian et al., 2016].

echo-cardiograms, chest x-rays, pulse oximetry, exercise stress tests, computed tomography or MRI scans, and cardiac catheterization. Treatment of different defects varies from monitoring and medication to surgery and cardiac implants.

The incidence of CHD in live births vary across countries and continents. The United States reports approximately 4-10 CHD case per 1000 live births. Europe and Asia see about 6.9 and 9.3 CHD cases per 1000 live births [Mozaffarian et al., 2016]. In China, the incidence of CHD ranges from 8.98 to 11.1 per 1000 live births [Zhao et al., 2019] [Qu et al., 2016]. A pair of studies from Iran report incidences of 8.6 and 12.3 per 1000 live births, though the studies note that they were performed in different geographical locations with different populations within the country [Nikyar et al., 2011] [Rahim et al., 2008]. One report from Dharan reports an incidence of 5.8 per 1000 patients admitted to a tertiary care hospital over a 12 month period [Shah et al., 2008]. A study of newborns at one hospital in New Delhi, India claims an incidence of 3.9 per 1000 live births, though this rate may be a poor estimate as there is a significant delay between patient birth and referral to a cardiac center

in India [Khalil et al., 1994] [Saxena, 2005].

These incidence rates should be analyzed with some caution. In many cases, the reported rates were based on medical records. Medical records are not always correct. Additionally, the only way for a person to have a medical record is for him to go to a medical center. Not everyone who has CHD is able to seek medical help, often because of their geographical locations or their income. Even if a patient is able to seek medical help, the availability of proper cardiac care varies between and within countries.

As screening tools become more effective and more widespread, it is expected that incidence rates will increase as defects are detected earlier. Generally, the earlier a defect is detected, the earlier it can be treated. Early detection and treatment means more CHD patients will live to adulthood. Currently, Webb et al. estimate that at least 12 to 34 million adults have CHD, and this number is expected to increase [Webb et al., 2015].

It is important to note that each defect type has a different prevalence, a different treatment plan, and different expected outcomes. A breakdown of prevalence rates of some of the most common lesion types can be seen in Figure 3. Once a patient is diagnosed with one of these defects, the specific nature of his case must be clearly documented. The documentation of CHD using the International Classification of Diseases, Ninth Revision, Clinical Modification (ICD-9-CM) has 25 high level codes representing various presentations of CHD, but these codes used alone are often not sufficient for describing a patient's true condition [Mozaffarian et al., 2016]. Additional ICD-9-CM codes should be used to communicate the finer details of a patient's condition.

The financial burden of CHD varies depending on the defect. Certain defects require complex, expensive surgical repairs while others can be treated with less expensive approaches [Mozaffarian et al., 2016]. The burden of CHD across the globe was outlined by Webb et al. Their figure illustrating the prevalence of CHD and the availability of funds with which to treat it can be see in Figure 4. As the overall mortality of CHD declines, the burden of CHD is expected to increase [Mozaffarian et al., 2016].

Unfortunately, the cost of treating CHD alone is not the only burden a patient must undergo. Patients with CHD are also at increased risk for heart failure and infections [Mozaffarian et al., 2016]. Children with CHD are at 19-fold risk for stroke compared to

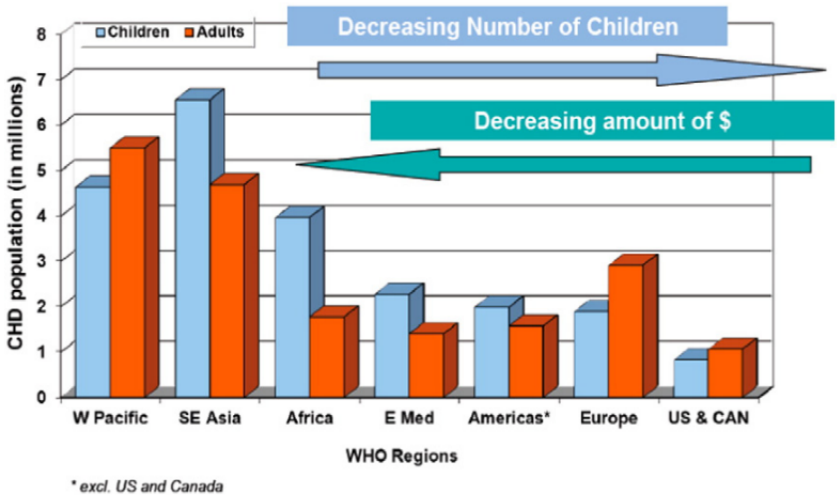

Figure 4: Estimated CHD burden in World Health Organization (WHO) regions using incidence rates of approximately 12/1000 and 4/1000 in children and adults, respectively [Webb et al., 2015].

their healthy counterparts [Fox et al., 2015]. In a study of Swedish citizens born between 1970 and 1993, Giang et al performed a study compared the prevalence of cardiac conditions in patients with and without CHD [Giang et al., 2018]. They found that patients who had a CHD diagnosis were at about eight times higher risk for intracerebral hemorrhage and subarachnoid hemorrhage than their non-CHD counterparts. The CHD patients were also more likely to suffer from arrhythmia and heart failure.

3.2 CHD AND NEUROCOGNITIVE DISORDERS

Cardiac conditions are not the only complications CHD must deal with. In recent years, researchers have found that there is a relationship between CHD and neurocognitive disorders.

3.2.1 Causes

Early research in this area focuses on the neurodevelopmental status of neonatal patients pre- and post-surgical intervention. One theory was that some factor or factors in the surgical intervention caused brain injuries in the patients. This idea proved to be inaccurate when researchers began detecting neurological malformations *in utero*.

In a systematic review of available literature regarding prenatal and postnatal presurgical CHD cases and neurodevelopmental outcomes, Mebius et al. identify two theories about the causality of neurodevelopmental delays and CHD [Mebius et al., 2017]. The first theory is that abnormalities in the cardiac system prevent the developing brain from receiving enough oxygen and nutrients, which disrupts prenatal brain development. The second theory is that faulty genetic pathways used during both cardiac and brain development cause both conditions to co-occur. However, 11 articles Mebius et al. found during their review that are related to bloodflow through the umbilical artery suggest a third theory. During the prenatal period, a fetus receives oxygen from the mother via the placenta. If the placenta was not functioning correctly, it could lead to the fetus receiving not enough oxygen. Lower quantities of oxygen throughout prenatal development could potentially cause problems both in brain and cardiac growth. The 11 articles have contradictory results, but some researchers are currently investigating the role of the placenta in CHD and prenatal brain development.

3.2.2 Aging

Survival of CHD patients to adulthood has increased from 10% to 90% over the last several decades. The impact of the combination of CHD and neurological conditions throughout a patient's lifetime is starting to be explored. The aging of the CHD population has also sparked interest in the relationships between CHD and adult-stage neurological disorders such as dementia and Alzheimer's.

3.3 IDENTIFYING NEUROCOGNITIVE DISORDERS

3.3.1 Patient Surveys

Surveys known to be used for studying the relationship between CHD and neurodevelopment are

- National Institute of Health Toolbox (3 - 85 years): "Performance tests of cognitive, motor, and sensory function and self-reported measures of emotional function for adults and children in the general population and those living with a chronic condition".
- Sue Beers (4 - 18 years [not inclusive of 18 years]): WASI-II, NEPSY-2, WRAML-2, D-KEFS, WISC-IV, Grooved Pegboard, BRIEF, Beery-Buktenica VMI, ASRS, Conners-3, BASC-II, ABAS-II, PedsQL General, PedsQL Cardiac, Pictoral Scale Self Perception Profile.
- SVR-III NDT (9 - 13 years [not inclusive of 13 years]): WIAT, NEPSY, WRAML, D-KEFS, WISC-V, Grooved Pegboard, BRIEF, Beery-Buktenica VMI, ASRS, Conners ADHD Index, BASC-II, ABAS-3, PedsQL General, PedsQL Cardiac
- Bayley Scales of Infant and Toddler Development -III (1 - 24 months): Subtests include cognitive, language, social-emotional, motor, and adaptive behavior tests [Mebius et al., 2017].
- Battelle Developmental Inventory (Birth - 8 years [not inclusive of 8 years]): Subsets include cognition, communication, social-emotional development, physical development, and adaptive behavior.
- Developmental Assessment of Young Children (Birth - 6 years [not inclusive of 6 years]): Subtests include cognition, communication, social-emotional development, physical development, and adaptive behavior.
- Preschool Language Scale + Receptive-Expressive Emergent Language (Birth - 3 years): Total language, auditory comprehension, expressive communication, articulation, receptive language, expressive language, and inventory of vocabulary words.
- Peabody Developmental Motor Scales (Birth - 5 years): Subtests include reflexes, stationary, locomotion, object manipulation, grasping, visual-motor integration

The goal of these surveys is to compare the patient's cognitive function and neurological functions to expected milestones. Certain deviations from certain milestones are indicative of different disorders.

3.3.2 Neurological Images

When an area of the brain is active, it uses more oxygen than the surrounding regions. Functional MRIs (fMRI) are sensitive to signals emitted by deoxygenated hemoglobin. The blood oxygen level dependent (BOLD) signal recorded by the fMRI reveal regions of the brain which are active at the same time. These combinations of regions are called neuronal networks.

Many neuronal networks exist, but most of them are considered to be task related. In 2001, Raichle et al. suggested the existence of a neuronal network which operated when a person is at rest [Raichle et al., 2001]. Their theory was confirmed by Greicius et al. in 2003 [Greicius et al., 2003]. Because the patient is not performing a specific task when they are in a resting state, the resting-state networks have the potential to reveal valuable information about a patient's neurodevelopmental status.

A fMRI taken of a patient in a resting, task-free state, is called a resting-state fMRI (rs-fMRI). rs-fMRIs are sequences of image volumes acquired over a period of a few minutes. The image volumes themselves have relatively low spatial resolution when compared to structural MRIs, but their temporal resolution is significantly higher as a new volume is acquired every two to three seconds.

The BOLD signals in rs-fMRI image sequences are analyzed using a process called functional connectivity analysis. Functional connectivity analysis identifies patterns and networks of brain activity. Some functional connectivity analysis studies have lead to the discoveries of links between specific disruptions in these naturally occurring networks and neurodevelopmental diseases such as autism and attention deficit hyperactivity disorder [Assaf et al., 2010] [Zang et al., 2007]. With further refinements of both acquisition techniques and characterization of these functional networks, clinicians may be able to use rs-fMRI to evaluate the neurodevelopmental status of CHD patients and to identify patients

who may benefit from certain therapies or neuroprotective interventions.

3.4 SUMMARY

CHD consists of a variety of defects affect the vessels and chambers of the heart. It has a worldwide prevalence of about 8 per 1000 live births, meaning about 1.35 million children are born with CHD every year. Since the survivability of CHD has increased from 10% to 90%, the medical community is faced with a growing, aging population of CHD patients. Many of these patients also suffer from neurocognitive disorders that co-occur with CHD. The neurocognitive disorders are usually diagnosed using at least one of many psychological survey-based evaluations, but these methods are subjective. rs-fMRIs could be used to identify patients who have functional connectivity patterns associated with different neurocognitive disorders, and eventually may be used to identify patients who are at risk for developing these disorders.

4.0 METHODS: MOTION CORRECTION

In the previous chapter, we discuss several techniques used to retrospectively correct motion. Motion correction pipelines may use denoising and filtering, but all pipelines begin with volume registration. In this chapter, we discuss a different approach to volume registration, how it compares to traditional volume registration, and how volume registration fits into a motion correction pipeline.

4.1 DIRECTED ACYCLIC GRAPH BASED VOLUME REGISTRATION

As discussed previously, the major drawback to Friston et al.'s approach to volume registration is that it only minimized the positional differences between the reference volume and the rest of the sequence. This drawback demonstrates an inability for the traditional approach to account for relationships in the patient's position throughout the scan. Intuitively, we know that the patient's position at any volume in the scan is more similar to his position in the immediately previous or subsequent volume than to another randomly chosen volume in the image.

In our proposed framework, we wish to account for these spatiotemporal relationships between temporally neighboring volumes in the sequence. To accomplish this goal, we start by viewing the rs-fMRI sequence as a directed acyclic graph (DAG). A DAG consists of a set of nodes and edges. Each edge has a direction associated with it and connects a pair of nodes. Since a DAG contains no cycles, there is no possible path back to a node once it has been traversed.

In the case of an rs-fMRI, each volume can be considered a node. The relationship

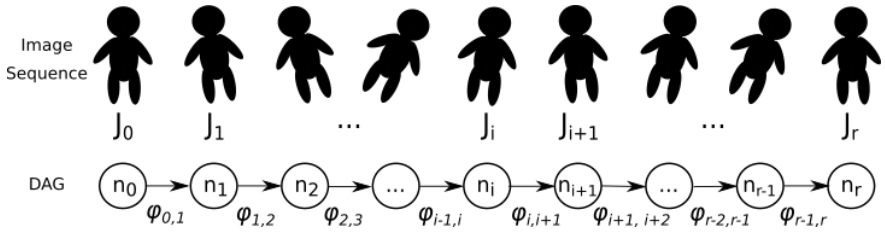

Figure 5: A rs-fMRI can be viewed as a directed acyclic graph where each volume is a node and the edges connect from each volume i to the following volume $i+1$.

between each pair of temporally neighboring volumes is represented as a directed edge connecting the node for the first volume to the node for the next volume. The acyclic nature of the DAG means that once a patient was in a specific position, he will never return to that exact same position with the exact same neurons firing. The position of the subject and his brain activity as measured by the BOLD signal may be similar in subsequent image volumes, but it will never be precisely the same. The perspectives of an rs-fMRI sequence as a set of images and of the sequence as a DAG can be seen in Figure 5.

The cost of transitioning from one node to the next in our DAG has a parallel representation to the combination of the positional transformation needed to align volume i to volume $i+1$ and the signal change between the volumes. This representation can be written as

$$J_{i+1} = \phi_{i,i+1} J_i + \delta s_{i,i+1} + \epsilon \tag{4.1}$$

where J_i and J_{i+1} are volumes i and $i+1$, $\phi_{i,i+1}$ is a matrix of transformation parameters that must be applied to J_i to achieve the patients position in J_{i+1}, $\delta s_{i,i+1}$ is the natural change in BOLD signal, and ϵ is the change in BOLD signal due to motion. Currently, there is no way to estimate the natural change in BOLD signal and the change in BOLD signal due to motion without incorporating additional information about the MRI scanner and the patient that is not included in a rs-fMRI. We simplify our representation of the relationship

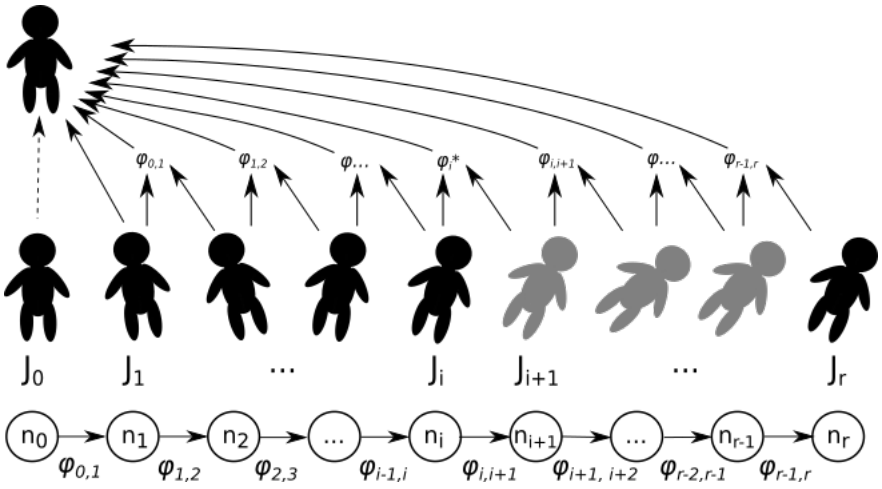

Figure 6: The traditional approach to volume registration in an rs-fMRI sequence consists of registering all volumes in the sequence to a single reference volume.

between two volumes to

$$J_{i+1} = \phi_{i,i+1} J_i + \epsilon^* \tag{4.2}$$

where ϵ^* is the change in the BOLD signal that cannot be accounted for after aligning the patients position in the two volumes. Here, we use the notation ϵ^* to represent the generic error change in BOLD signal across any pair of volumes.

After aligning two volumes i and $i+1$, we will then align volumes $i+1$ and $i+2$:

$$\begin{aligned} J_{i+2} &= \phi_{i+1,i+2} J_{i+1} + \epsilon^* \\ &= \phi_{i+1,i+2}(\phi_{i,i+1} J_i + \epsilon^*) + \epsilon^* \\ &= \phi_{i+1,i+2}\phi_{i,i+1} J_i + \epsilon^{*'} \end{aligned} \tag{4.3}$$

Traditional volume registration assumes that

$$\phi_{i,i+2} = \phi_{i+1,i+2}\phi_{i,i+1} \tag{4.4}$$

and calculates $\phi_{i,i+2}$ directly. We argue that this assumption is not true in all cases. Rather than directly calculate $\phi_{0,i}$ and use it to align volume i to the reference volume as the traditional method does, we calculate each component ϕ that is a factor of $\phi_{0,i}$. Each component $\phi_{i,i+1}$ is combined with the preceding $\phi_{0,i}$s to recursively align volume $i+1$ to the reference volume without making the large and often inaccurate transformations required by directly calculating $\phi_{0,i+1}$. This process is outlined in Figure 6.

4.2 INDEPENDENT COMPONENT ANALYSIS

The purpose of image registration is purely to ensure the position of the patient throughout the entire rs-fMRI is consistent. After registration, the image still contains BOLD source signals and noise signals caused by factors other than brain activity. The challenge of separating these combined signals is called blind source separation (BSS).

We chose to focus on an independent component analysis (ICA) approach for solving the BSS problem. The specific technique we use has been described by Beckmann and Smith as probabilisic ICA. This section aims to provide an overview of the probabilistic ICA technique. For further details, please refer to the technical reports by the FMRIB group [Beckmann and Smith, 2004] [Woolrich et al., 2004] [Beckmann et al.,] [Smith et al., 2004].

Probabilistic ICA is a linear regression model which performs mixing in the original data space and assumes the true BOLD signal has been confounded by Gaussian noise. These constraints mean that BSS can be solved in three steps:

1. Estimate a joint subspace consisting of source and noise signals and an noise subspace orthogonal to the joint subspace,
2. Estimate the independent sources in the joint subspace, and
3. Assess the statistical significance of the independent sources.

Probabilistic ICA treats the voxel intensity values in every frame of the image sequence as a matrix of V voxels across n time points. For each voxel $v_i \in V$, the observed signal in

that voxel can be modeled as

$$\vec{x_i} = A\vec{s_i} + \mu + \vec{\eta_i} \tag{4.5}$$

This equation allows three different types of signals to contribute to the observed voxel values $\vec{x_i}$ for a given voxel across all n timepoints in the sequence. The first type of signal is a vector of non-Gaussian source signals $\vec{s_i}$ across all n timepoints. The source signals are modulated by mixing matrix A whose shape is the number of time points n by the number of source signals q. The second type of signal is an offset denoted by μ. The offset constrains the observed signals to be centered around the mean of all observed signals. The third type of signal $\vec{\eta_i}$ is a vector of noise throughout the duration of the sequence. To summarize, probabilistic ICA explicitly assumes that the observed signal in a given voxel can be divided into non-Gaussian source signals, isotropic Gaussian noise signals, and some offset. This assumption makes it easier to separate a source signal from a noise signal: a noise signal will have a Gaussian distribution while a source signal will not. **The goal of probabilistic ICA is to identify the source signals, $\vec{s}$.**

With this combination of signals in mind, we can write the covariance matrix of the observed data x as

$$R_x = \langle x_i x_i^T \rangle = AA^T + \sigma^2 I \tag{4.6}$$

where A is the mixing matrix, σ^2 is the standard deviation of the noise, and I is nxn identity matrix. The covariance matrix of the observed data R_x can be calculated, but A and σ^2 are both unknown. The noisy observed data is transformed with respect to the noise sources using a process called whitening. The whitening with respect to noise enforces the assumption of noise following an isotropic Gaussian distribution with a mean of zero and a standard deviation of σ^2.

The mixing matrix A can be estimated using maximum likelihood estimation. Beckmann and Smith use singular value decomposition of the observed data $X = U(N\Lambda)^{\frac{1}{2}}V$ to model the estimator of A:

$$\hat{A}_{ML} = U_q(\Lambda_q - \sigma^2 I_q)^{\frac{1}{2}}Q^T \tag{4.7}$$

where U_q contains the eigenvectors associated with the q largest eigenvalues, Λ_q contains the q largest eigenvalues, and Q is a qxq orthogonal rotation matrix in the whitened observation space such that $QQ^T = I$. The eigenvectors and eigenvalues can be calculated from X, but σ and Q remain unknown. As noted earlier, the matrix Q is an orthogonal rotation matrix which, when applied to the whitened data $\tilde{x}$, has the same effect of applying an unmixing matrix to the observed data:

$$W\vec{x} = Q\tilde{x} = \hat{s} \tag{4.8}$$

Both matrix-vector multiplications serve to estimate individual source signals $\hat{s}$. The estimated source signals are identified by projecting the whited data $\tilde{x}$ onto each row r of the unmixing matrix Q a total of q times:

$$\hat{s_r} = Q_{r,:}\tilde{x} \tag{4.9}$$

where the $Q_{r,:}$ represents row r of matrix Q. *(Note: A key assumption in this step is that the rows of the unmixing matrix are mutually orthogonal so that they cover the entire space of signal sources. Additional steps described by Beckmann and Smith can be taken to incoporate prior information about the voxels into this step [Beckmann and Smith, 2004].)*

At this point, the standard deviation of the noise σ^2 and the source signals are unknown. We can solve the following system of equations jointly to resolve these two unknown quantities:

$$\hat{s}_{ML} = (\hat{A}^T\hat{A})^{-1}\hat{A}^T x = \hat{W}x = Q\tilde{x} \tag{4.10}$$

$$\hat{\sigma}^2_{ML} = \frac{1}{n-q}\sum_{l=q+1}^{p}\lambda_l. \tag{4.11}$$

Solving these equations is an iterative process. First, the mixing matrix and source signals are estimated. These estimations are used to calculate the corresponding estimator of the standard deviation of the noise. Then, the residual noise $\hat{\eta}_i$ at each voxel v_i is calculated:

$$\hat{\eta}_i = (I - \hat{W}^T\hat{W})x_i. \tag{4.12}$$

Recalling from Equation 4.5 how probabilistic ICA views a signal, Equation 4.12 becomes:

$$\hat{\eta}_i = (I - \hat{W}^T\hat{W})A + (I - \hat{W}^T\hat{W})\eta \tag{4.13}$$

When the correct number of sources has been identified, the estimated mixing matrix will fully span the source signal space. Then, the residual noise will only be related to the true noise:

$$\hat{\eta}_i = 0 + (I - \hat{W}^T\hat{W})\eta \tag{4.14}$$

Upon reaching this stage in the probabilistic ICA technique, the source signals have been approximated. The source signals are called spatial independent component maps. Normalizing the values in these maps by the variance of the noise produces Z-statistic maps. Z-statistic maps can be analyzed to identify voxels with statistically significant activations. These activations are attributed to BOLD signal.

One of the major limitations of ICA is that it is highly data driven. It assumes the dataset contains a sufficiently large number of images, each with a sufficiently large number of voxels. Even assuming an ideal data set, the true value of the mixing matrix is dependent on the observed data [Beckmann and Smith, 2004]. Fluctuations in the data can lead to deviations of the residual noise in certain voxels from the true noise. These deviations can produce *type-I* and *type-II* errors when examining the Z-statistic maps to identify statistically significantly activated voxels.

Additionally, the developers of probabilistic ICA note that not all noise follows the isotropic Gaussian assumption. Noise based in the patient's physiology is likely to be structured in a way that is non-Gaussian. The non-Gaussian noise signals can still be separated from the BOLD source signals, but only if these noise signals are not highly correlated with the source signals.

4.3 MOTION CORRECTION PIPELINE AND IMPLEMENTATION

Both the traditional and novel volume registration techniques were applied independently to each image from the subject cohorts described in Chapter 6. After registration, three versions of each image existed: the original BOLD sequence, the sequence modified using traditional volume registration, and the sequence modified using the novel registration method.

The registration algorithms applied to rigid tissue types used affine registration with two degrees of granularity. When applied to soft tissue types (ie, placenta), three nonlinear transformations with increasing granularities were performed after the affine registrations. The exact parameters used for each volume registration can be seen in Appendix A. The registration frameworks were implemented in Python using the nipype (Neuroimaging in Python Pipelines and Interfaces) library [Gorgolewski et al., 2011]. Volume registration used the ANTs (Advanced Normalization Tools) tools as a backend [Avants et al., 2014].

After performing volume registration to ensure the patient is in the same physical space throughout the image sequence, the image sequence may still contain artifacts due to motion. Our registered sequences underwent motion correction via a well-established motion correction pipeline. We chose to use the independent component analysis (ICA) pipeline outlined by Beckmann and Smith [Beckmann and Smith, 2004]. The motion corrected sequences produced by FMRIB's MELODIC tool were saved alongside the original and registered sequences.

4.4 EVALUATING REGISTERED AND MOTION CORRECTED SEQUENCES AGAINST GOLD STANDARD USABILITY THRESHOLDS

The main goal of motion correction is to reduce the effects of motion on the image so that it is usable. The gold standards for rs-fMRI usability as established by Power et al. are that the FD and DVARs metrics must change less than 0.2 mm and 2.5% normalized voxel units between at least 50% of the neighboring volumes. The FD and DVARs metrics

between each pair of subsequent image volumes were calculated for the original, registered, and motion corrected sequences. The metrics for each sequence were then compared to the gold standard image usability thresholds. This comparison answers the key question of how each registration framework impacts an established motion correction pipeline.

Additionally, a smaller comparison of the registered sequences was conducted. This comparison evaluates the immediate impact of the registration algorithm on the image sequence. It is highly unlikely that an entire image sequence would meet the Power et al. usability thresholds after only the initial step of a motion correction pipeline, but it is valuable to examine the impact of a volume registration algorithm at each stage of the pipeline.

Implementation. We calculated the FD and DVARS metrics defined by Power et al. using the FSLMotionOutliers tool [Power et al., 2012].

5.0 METHODS: EVALUATING MOTION PATTERNS

In the previous chapter, we describe the methods we use to mitigate the positional effects of motion in rs-fMRI sequences. We briefly discuss how the motion corrected sequences were evaluated with respect to gold standard usability criteria. Here, we expand on our analysis of the motion extracted from the sequences.

5.1 MEASURING MOTION PATTERNS

While the Power et al. usability thresholds for the FD and DVARs metrics quantify the volume-to-volume motion well, they do not quantify the overall motion contained in the image sequence. The FD and DVARs metrics as well as other imaging metrics can be used to compare every volume in an image sequence to every other volume in the image sequence to better quantify whole-sequence motion. As the FD and DVARs metrics have been discussed previously, we will focus in this section on three other image metrics: the Dice coefficient, the correlation ratio, and the mutual information. These five metrics were applied to each whole sequence to measure patient motion and image signal consistency throughout the entire scan.

5.1.1 Dice Coefficient

The Dice coefficient was proposed by Lee R. Dice in 1945 [Dice, 1945]. Dice examined several existing metrics for measuring association, and finding them lacking, proposed his own "coincidence index". His coincidence index measures the association between a number

of samples a where condition A is true and a number of samples b where condition B is true:

$$Index = \frac{2h}{a+b} \tag{5.1}$$

In this equation, h represents the number of samples where both conditions A and B are true. His index can take on any value between 1.0 and 0.0 such that a value of 1.0 means that conditions A and B are true for all samples. Similarly, a value of 0.0 means that conditions A and B are never both true for any sample. While this index is a count of samples that meant both conditions and not a true probability, Dice suggests that the chi-squared test can be used to determine if the combinations of conditions in the samples from a set of data is meaningful or due to random chance.

Many medical imaging researchers have adapted the Dice coefficient to measure the overlap between pairs of images. Zijdenbos et al. trained an artificial neural network to semiautomatically segment brain MRIs and compared the generated segmentations to manual segmentations using the Dice coefficient [Zijdenbos et al., 1994]. Zou et al. used the Dice similarity coefficient in their analysis of the reproducibility of manually segmented MRIs and the accuracy of automatic segmentations of the same images for prostate and brain tumor datasets [Zou et al., 2004]. Liao et al. used it to measure the accuracy of a volume registration framework for aligning manual segmentations of multiple organs in fetal images [Liao et al., 2016]. Bharatha et al. performed a study on pre- and intra-operative images of the prostate. They segmented the images, generated deformable finite element models of the segmentations, and used the Dice coefficient to compare the registered segmentations and finite element models [Bharatha et al., 2001].

It should be noted that the Dice coefficient as used in these contexts is a measure of similarity of items from two categories where each item belongs to exactly one class. The two classes of interest in the case of rs-fMRIs are "brain" or "not brain". Medical images do not naturally have binary values. All studies mentioned in the previous paragraph require a domain expert to manually segment each image that will be analyzed using the Dice coefficient. The manually segmented images are considered the gold standard to which automatic segmentations or registered images can be compared.

The images in our dataset have been manually curated to remove the skull and other

anatomical features outside of it, but the images still contain a continuous range of voxel intensity values. The Dice coefficient cannot be directly applied to these image sequences, even though each voxel only belongs to one of two classes. The volumes first must undergo thresholding to create binary images to clearly separate brain and background for computational purposes. We use Otsu thresholding to accomplish this task.

Otsu thresholding divides the contents of an image into two binary classes based on the histogram of voxel intensity values. It assumes that the classes are represented in the histogram by separable peaks. It separates the peaks by finding the separation threshold with the best separation between classes. In its original form, Otsu thresholding exhaustively searches the space of all possible thresholds and calculates the within-class variance and between-class variance for the pair of classes separated by the current threshold option. The ideal threshold is the one which produces the minimal within-class variance and the maximal between-class variance. The ideal threshold is then used to convert the original image into a binary image volume where background voxels have a value of zero and voxels in the brain have a value of one. The binarized image volume can be compared to other binarized image volumes using the Dice coefficient.

In cases where a good Otsu thresholded binary image cannot be obtained, other similarity metrics such as mutual information and cross correlation should be used instead.

5.1.2 Correlation Ratio Matrix

The correlation ratio is an asymmetrical, spatially informed measure of the overlap between images. It is different from other similarity metrices in that a lower correlation ratio indicates a better alignment between two images rather than a worse alginment.

The earliest symbolic representation of the correlation ratio is

$$\eta = \frac{\Sigma}{\sigma_y} = \frac{\sqrt{\frac{\sum(n_x(\overline{y}_x - \overline{y})^2)}{N}}}{\sigma_y} \tag{5.2}$$

where n_x is the number of samples in any one set x, $\overline{y}_x$ is the average of the samples in x, $\overline{y}$ is the average of all samples in all sets, σ_y is the standard deviation of all samples in all sets, and N is the total number of samples across all sets [Rugg, 1917]. The meaning of

this equation was simplified by Ayres, who describes it as "the ratio between two standard deviations" [Ayres, 1920]. In Equation 5.2, the numerator is the standard deviation of a single set of samples with respect to all sets of samples, and the denominator is the standard deviation of all sets of samples. The process of calculating the individual components of this equation are outlined in [Rugg, 1917].

The correlation ratio was proposed for use in medical imaging applications in 1998 and compared to other similarity metrics. Roche et al. provide an example of algining two black images, one with a uniform gray stripe and the other with a horizontal gray gradient, such that the overlap between the two images is maximally similar [Roche et al., 1998a], [Roche et al., 1998b]. They show that the mutual information metric has a maximum value at every translation of an integer number of pixels while the correlation ratio had a maximum value at one single alignment. They apply the correlation ratio to MR images as well as computed tomography and positron emission tomography images. Their experiments suggest that in the context of multimodal registration, the correlation ratio balances accuracy and robustness.

In the context of medical imaging, the correlation ratio measures the functional dependence between a pair of images X and Y. The correlation ratio of Y given X is

$$\eta(Y|X) = \frac{Var[E(Y|X)]}{Var(Y)} \tag{5.3}$$

This equation is comparing the energy of Y in X to the total energy of Y. If X and Y overlap in area Ω, the number of pixels in that area is $N = Card(\Omega)$. Since X is known, it can be divided into sets of pixels Ω_i where each set is comprised of locations in Ω where the pixels X have the same value i.

Because the correlation ratio is a strong metric for measuring the similarity between two images, we suggest using it to quantify the similarity between all volumes in an image sequence. We choose to refer to this metric as the correlation ratio matrix. For a sequence of length l, the correlation ratio matrix M is a square, asymmetrical matrix of size $l * l$. Each

cell in M is calculated as

$$M_{i,j} = \eta(J_i, J_j) = \frac{Var[E(J_i|J_j)]}{Var(J_i)} = \frac{\sqrt{\frac{\sum |J_i|(\overline{J_i} - \overline{J_i \cap J_j})^2)}{|J_i \cap J_j|}}}{\sigma_{J_i \cap J_j}} \tag{5.4}$$

where J_i and J_j are volumes $i \in l$ and $j \in l$ in the sequence, respectively. The sequence $J_i \cap J_j$ is the volume of space where images J_i and J_j intersect. The equation measures two different properties of the volume spaces J_i, J_j, and $J_i \cap J_j$: the number of voxels and the average of the voxel values in the space. The symbol $|.|$ indicates the number of voxels the specified space, and the symbol $\bar{.}$ indicates the average of the voxel values in the specified space.

Since the matrix M is quite large, using statistics describing M rather than M itself can simplify analyses. On the other hand, the whole matrix M can be more comprehensively analyzed using statistical tests such as the t-test.

5.1.3 Mutual Information

The earliest description of mutual information was written in the context of mathematical theories behind networked communication [Shannon, 1948]. Mutual information is a measure of the amount of information shared between two signals X and Y. Specifically, mutual information measures how the joint distribution of the two signals compares to the marginal distribution of each signal [Li, 1990]. It is a more general measure of dependence than correlation, which is limited to measuring linear dependence via a comparison of the marginal distributions. In terms of information theory, mutual information is represented as

$$MI(X, Y) = H(X) + H(Y) - H(XY) \tag{5.5}$$

where $H(X)$ is the entropy of signal X

$$H(X) = -\sum_{x \in X} p_x log(p_x) \tag{5.6}$$

where p_x is the marginal distribution of the signal X. Substituting y for x in this equation produces $H(Y)$, the marginal entropy of the signal Y. Similarly, $H(XY)$ is the joint entropy

of signals X and Y given the known signals X and Y

$$H(XY) = -\sum_{x \in X, y \in Y} p_{xy} log(p_{xy}). \tag{5.7}$$

It is worth noting that since the two signals of interest are registered images, x and y refer to voxel locations in the same image space. Substituting Equations 5.6 and 5.7 in Equation 5.5 produces the following

$$\begin{aligned} MI(X,Y) &= -\sum_{x \in X} p_x log(p_x) - \sum_{y \in Y} p_y log(p_y) + \sum_{x \in X, y \in Y} p_{xy} log(p_{xy}) \\ &= \sum_{x \in X, y \in Y} p_{xy} log p_{xy} - \left(\sum_{x \in X} p_x log(p_x) + \sum_{y \in Y} p_y log(p_y) \right) \end{aligned} \tag{5.8}$$

In the case where signals X and Y are independent, Equation 5.8 can be simplified to

$$\begin{aligned} MI(X,Y) &= \sum_{x \in X, y \in Y} p_{xy} log(p_{xy}) - \left(\sum_{x \in X} \sum_{y \in Y} p_{xy} log(p_x p_y) \right) \\ &= \sum_{x \in X, y \in Y} p_{xy} log \left(\frac{p_{xy}}{p_x p_y} \right) \end{aligned} \tag{5.9}$$

Mutual information can be used to determine how the distribution of amplitudes in one signal relates to the distribution of another signal. It is commonly used in the medical imaging domain to objectively compare images of the same tissue taken using different modalities. For example, a computed tomography (CT) scan of a patient's abdomen contains different information about each tissue types' material properties than an MRI of the same organs. Some tissue types may appear similar in one of these modalities but drastically different in the other. Combining the information about a tissue's material properties gained from both imaging modalities provides more information than could be gained from either modality independently. (In other words, the resulting information is greater than the sum of its parts.)

Even though the rs-fMRIs in our study are all obtained using the same imaging modality, the spin history effects of patient motion can impact the recorded signal such that small changes in recorded BOLD signal are difficult to distinguish from noise due to motion. We

choose to use mutual information to quantify to BOLD signal information across the entire image sequence.

5.1.4 Implementation: Tools and Libraries

To calculate metrics, we used several existing tools and libraries. When no existing tool could be found, functions were implemented manually in Python3.

For the Dice coefficient calculation, we first had to create a binary version of each image volume. To binarize the image volumes, we used Simple ITK's Otsu thresholding function. The binary images were then passes to a manually implemented function to calculate the Dice coefficient.

The correlation ratio between each possible pair of volumes in the sequence was calculated using bash and FLIRT (FMRIBs Linear Image Registration Tool) [Jenkinson and Smith, 2001] [Jenkinson et al., 2002]. We then used the average and standard deviation of the correlation ratio distribution of each image to compare the images.

The mutual information calculation was implemented in two steps. The first step was to create a function that computes the joint histogram of the voxel value distributions between the two image volumes. This histogram was fed to a second function that converts the histogram counts to probabilities and calculates the mutual information value.

5.2 PATIENT CLASSIFICATION USING MOTION PATTERNS

We suggest that the ways that patients move are specific to certain age groups. For example, fetal patients live suspended in amniotic fluid and as such are subject to different physical constraints than patients in other age groups. Neonatal patients are often scanned using a "feed and bundle" protocol, which often results in them sleeping through the scan. However, neonatal patients sometimes wake up during the scan, and the way a baby woken up from a nap moves is different from how a fidgety preadolescent moves.

There is also a chance that patients within the same age group move differently possibly

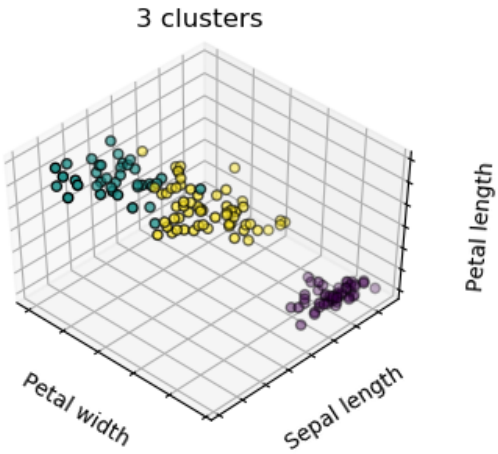

Figure 7: An example of k-means clustering performed on the Iris data set. The results of the algorithm are highly dependent on the number of clusters specified.

due to their cognitive state. Preadolescents who have ADHD likely become bored and fidgety in the MR scanner at different rates then their non-ADHD counterparts. Adults suffering from dementia may have more difficulty remaining still for the duration of a scan than adults from similar demographics with no dementia.

These patterns are essentially signals specific to different categories of patients. Machine learning techniques are useful for identifying patterns in signals from different sources. In addition to the motion metrics identified in the previous section, we will also use demographic and clinical data as features for our machine learning models.

The goal of applying machine learning to identify population level motion patterns lends itself well to unsupervised machine learning techniques. Unsupervised learning techniques group samples from a population based on the patterns in their features. They do not use information about any known groups in the population to inform their classification processes. In this section, we discuss several different unsupervised machine learning techniques used to measure degrees of association within subgroups of a data set.

5.2.1 K-means Clustering

K-means clustering divides a group of data samples with n features into k groups based on each sample's distance from the average value of the group [Hartigan and Wong, 1979], [MacQueen, 1967]. In k-means clustering, the features of a set of data are viewed as the locations of each data sample in n-dimensional space. In this space, k cluster centroids are initially distrubuted. The distribution pattern can place the centroids either randomly between data samples or using randomly selected data points.

After the locations of the cluster centroids are initialized, the distance between each sample and each centroid is calculated. Each sample is assigned to the cluster represented by the centroid closest to it. Once the clusters are defined, the location of the centroid of each cluster is recalculated. The new centroid location is the mean of the locations of all samples in its cluster. The distance between each sample and each cluster centroid is recalculated, samples are reassigned to their closest cluster centroid, and the centroid of each cluster is recalculated. This process continues until a stopping criteria is fulfilled. With most unsupervised machine learning methods, the stopping criteria is that the classifications of the model do not change for a certain number of iterations. However, a maximum number of iterations is imposed on the learning process to prevent a model from running indefinitely. As a result, it is possible for a model to "time out" before reaching a stable state.

There are many variations of k-means clustering. For example, k-medians follows the same steps as k-means, but uses the median of the known data points in a cluster as the new centroid for that cluster [Juan and Vidal, 1998]. Another variation called k-mediods uses the data point closest to the center of the cluster as the new cluster centroid rather than a descriptive statistic of the cluster [Kaufman and Rousseeuw, 1987].

One of the major limitations of k-means clustering is that the number of clusters must be given to the model. It is difficult to know how many clusters are needed to adequately represent subgroups within a data set. If too many clusters are used, the groups identified by the algorithm will be more granular than they should be; however, using too few clusters will produce large groups which mask distinct subgroups. An example of k-means clustering as applied to the Iris data set can be seen in Figure 7 [Varoquaux, 2019]. The results of the

clustering are dependent on the number of clusters specified as well as the points used to initialize the algorithm.

5.2.2 Spectral Clustering

While spectral clustering is related to k-means clustering, it approaches the problem of identifying associations in a group of data from a different perspective. Spectral clustering treats each data point in a sample as a node in a graph. The connections between data points are characterized by the adjacency matrix and the degree matrix of the graph. These two matrices are used to calculate the Laplacian matrix of the graph, whose properties are used to identify clusters. All three matrices are nxn matrices, where n is the number of data points in the sample.

Herein, we discuss spectral clustering when the data can be represented using a simple graph. As such, certain mathematical shortcuts can be employed to simplify certain computations. A more general mathematical approach has been discussed by Ng, Jordan, and Weiss [Ng et al., 2002].

The adjacency matrix specifies the strength of the connection between the nodes represented by the rows and columns of the matrix. For data that does not begin in graph form, algorithms such as k-nearest neighbors can be used to generate the adjacency matrix. In the adjacency matrix, each entry i, j contains the weight of the connection between node i and node j. If the edges are unweighted, the value of the entry is either 0 or 1. If the graph is undirected, the value of entry i, j is the same as the value of entry j, i. All entries where $i = j$ should be 0, unless node i has a self-loop.

The degree matrix is a diagonal matrix which represents the number of edges connected to each node. If the graph is directed, the directionality of the degree matrix must be specified: a directed connection from node a to node b contributes to the count for node a if the degree matrix counts the number of edges that begin at each node (outdegree), but contributes to the count for node b if the degree matrix counts the number of terminating edges at each node (indegree). In the case of an undirected graph, the connections include all edges that begin or terminate at a node. To summarize, in an directed graph, each edge

contributes to only one node count while in an undirected graph each edge contributes to both nodes.

The adjacency matrix and the degree matrix are used together to construct the Laplacian matrix of the graph. This calculation of the normal Laplacian for a simple graph (undirected and containing no loops) is straightforward: the adjacency matrix is subtracted from the degree matrix. The resulting matrix has the following properties:

- The diagonals are the number of connections per node less the number of self-connections
- All off-diagonal values are the negative of the weight connecting node i to node j.

It is important to note that if the graph in question contains loops or is directional, other methods must be used to calculate the Laplacian matrix.

The Laplacian matrix can be used to explore many properties of a graph. In particular, the eigenvalues of the Laplacian matrix are informative about the number of connected components in the graph. Connected components are areas of the network that are connected to each other but not anything outside that component. Each connected component is not its own cluster, though: the connected components could be large and contain smaller sets of connected nodes that are good options for clusters.

To determine the number of clusters in the graph, the eigenvalues of the Laplacian matrix are sorted in increasing order. The number of zero-valued eigenvalues is the number of connected components in the graph. Eigenvalues close to zero suggest weak edges preventing some connected component from being two separate components. Manually examining these eigenvalues before performing spectral clustering can be informative about the number of clusters to create: the number of values below the first large gap between the eigenvalues are the number of clusters, k. The eigenvectors associated with these k eigenvalues are used as a lower-dimensional representation of the data in the graph. Performing k-means clustering on this data produces the labels for the clusters within the data that are not linearly separable otherwise.

The limitations of spectral clustering are strongly related to the process of remapping the data to a lower dimensional space. When reducing the number of features used to represent a data set, information about that data set is inherently lost. The missing information

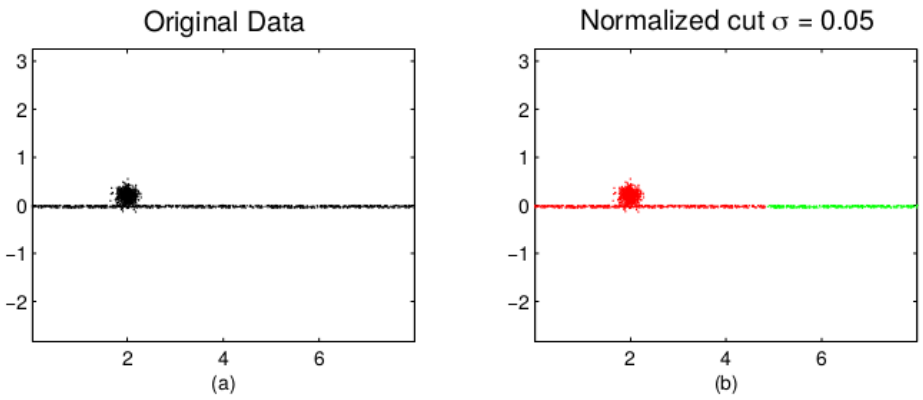

Figure 8: (a) Two different distributions, a 2D Gaussian density and a thin horizontal rectangle are difficult to separate (b) due to their overlap and the penalties built into the cost function of the spectral clustering algorithm. From [Nadler and Galun, 2007].

can make separating classes in the lower dimensional data significantly more difficult, if not impossible. Consider the following two cases: a case where two classes overlap and a case where three classes are unevenly represented in the data.

In cases where two seemingly obvious clusters overlap, the clustering algorithm may be unable to accurately identify them due to the mathematical penalties imposed on separating points in the feature space. An example of this problem as described by Nadler and Galun can be seen in Figure 8 [Nadler and Galun, 2007]. The two distinct groups are the small 2D Gaussian density and the horizontal rectangle. The spectral clustering algorithm (in this case, the normalized cut algorithm) is unable to separate the groups because the degree of overlap between the Gaussian density and the rectangle is greater than the height of the rectangle. It is more cost-effective for the algorithm to make a vertical cut to divide the rectangle in two than to cut the Gaussian density away from the rectangle.

Uneven distributions of data classes can severely impact spectral clustering results. Consider the case where a data set contains one highly populated class with a wide variation in its data's features and two less populated classes with less variation in their data's features. The scale of the large, highly populated class can overshadow the smaller classes: if the three

most important eigenvectors are more related to the large class than the smaller classes, the algorithm will not be able to differentiate between the two smaller classes.

5.2.3 Agglomerative Clustering

Agglomerative clustering is a specific type of hierarchical clustering which builds a tree of similarities between data samples from the "bottom up" [Ward, 1963]. The data samples in agglomerative clustering are also viewed as distinct points in n-dimensional space, but the number of groups to identify is not specified.

First, the distance from every data sample to every other data sample is calculated. The two data points that are closest together in terms of some similarity metric are combined into a single cluster. In the relationship tree representing the similarities between all data samples, a node is created and the joined data points are connected to that node. That node or cluster is treated as an intermediate data sample. The distance from the new "data sample" to every other data sample is calculated and the two closest data samples are again combined into another intermediate sample. A node representing the new cluster is added to the relationship tree and the data sample or samples merged into the cluster are connected to the node. The process of combining data points into clusters based on similarity to other data points terminates when all data points and clusters have been combined.

The results of agglomerative clustering can be interpreted by traversing the relationship tree. The relationship tree recorded the history of which nodes were merged into which clusters at each stage. Due to the nature of agglomerative clustering, these stages can be viewed as distinct levels in the tree. Beginning at the final node (the root) of the tree, the granularity of the clusters can be explored. At the top level, there is only one cluster, but at the second to last level of the tree there will be two clusters, at the third level there will be three clusters, and so on. How each cluster grew can reveal information about the relationships between the data samples within that cluster.

Agglomerative clustering also lends itself well to visualization via heatmap. The heatmap allows the researcher to see the distribution of feature values across the dataset and across visually prominent clusters. The Python library **seaborn** has a function called **clustermap**

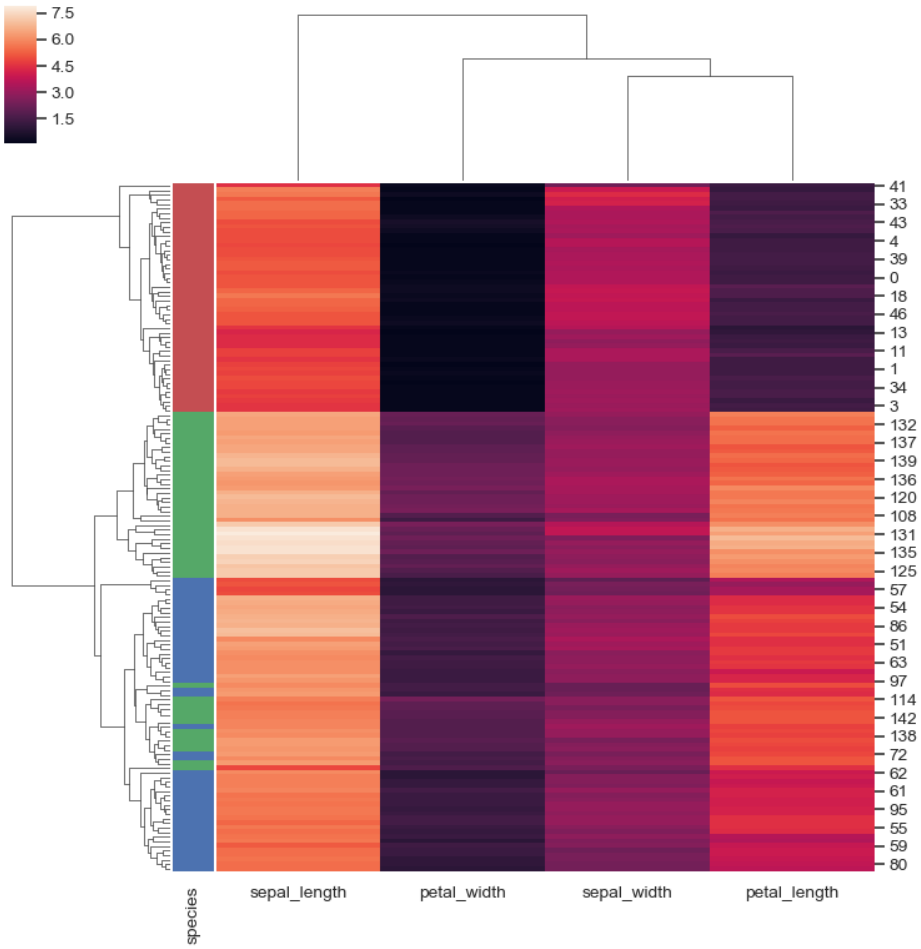

Figure 9: An example of agglomerative clustering on the Iris data set plotted using **seaborn**'s **clustermap** function.

which both performs agglomerative clustering and shows the resulting trees in a structured heatmap. An example of agglomerative clustering from the **seaborn** documentation where the clustering was applied to the Iris data set can be seen in Figure 9 [Waskom, 2018]. Each column represents a feature and each row represents a single sample. The colorbar in the top left of the figure shows that lighter colors in each cell represent higher values. The dendrogram along the top of the heatmap shows the distance between each feature. The dendrogram along the left of the heatmap shows the distance between each data sample and the data sample most similar to it. The column immediately to the right of this dendrogram shows the known class (species) for each data sample. The class labels in conjunction with the dendrogram of the data samples show the distinct groups present in the data which were identified using agglomerative clustering.

5.2.4 Visualizing Clustering Results

The results of unsupervised clustering algorithms can be visualized to illustrate how the computer chose each group of samples. Depending on the number of features n for each data sample, a dimensionality reduction method may be needed to transform the location of the data sample in n-dimensional feature space to a more easily visualized 2-dimensional or 3-dimensional space. The three dimensionality reduction methods we consider are principle component analysis (PCA), T-distributed stochastic neighbor embedding (t-SNE), and uniform manifold approximation and projection (UMAP).

PCA. Principle component analysis is a multivariate statistical technique that can be used to transform a set of variables with some degree of intercorrelation into a set of new, independent, orthogonal variables [Abdi and Williams, 2010]. These variables are called principle components of the data set. The principle components are ordered with respect to the amount of variance in the data set that can be projected onto each component. In general, PCA fits an p-dimensional ellipsoid to a data set with n features such that $p < n$. Each axis of the ellipsoid represents a single principle component. The first two or three principle components can be used to plot the results of a clustering algorithm in 2D or 3D space.

It is important to note that prior to the application of PCA, the data must be normalized. Normalizing the data allows different features to be compared on the same scale.

t-SNE. T-distributed stochastic neighbor embedding (t-SNE) was developed by Maaten and Hilton to perform nonlinear dimensionality reduction for visualizing high-dimensional data in a 2D or 3D space [van der Maaten and Hinton, 2008]. The algorithm first constructs a distribution of the high-dimensional data to measure the pairwise similarity of all data points. It also constructs a second distribution to measure the pairwise similarity of the data points in the lower dimensional space. Then, it performs gradient descent to minimize the difference between the two distributions as measured by the Kullback-Leibler divergence. At each iteration of the gradient descent, the distribution of points in the lower dimensional space is modified. The algorithm converges when the distribution of pairwise similarities between data points in the lower dimensional space most closely matches the corresponding distribution in the original high-dimensional space.

t-SNE is a computationally expensive technique with a complexity of $O(N^2)$ where N is the number of data points. For this reason, it is recommended that data with more than 50 features undergo another form of dimensionality reduction before t-SNE is applied to a data set. Even when this recommendation is not followed, the lower dimensional data produced using t-SNE lacks the interpretability of PCA data: the resulting dimensions have no interpretable meaning.

UMAP. Uniform manifold approximation and projection (UMAP) was proposed as an alternative to t-SNE [McInnes et al., 2018]. Rather than build a pairwise similarity distribution, UMAP uses topological representations of the data. For each point x_i, the distances between x_i and its k nearest neighbors are measured and normalized by the distance between x_i and the kth neighbor. These collections of distances around each point are local manifolds. The local manifolds are combined into the same global manifold using fuzzy simplical sets. After the global of the data is known, it is used to determine where data points must lie in a lower dimensional space so that they both adhere to the known manifold topology and retain the distance metrics from their k nearest neighbors. The topology of the lower dimensional manifold is adjusted iteratively to minimize the cross-entropy between the higher dimensional representation and the lower dimension representation. In practice,

UMAP treats each data point as a node in a weighted graph. It first determines each point's k nearest neighbors and calculates the distances between them, and then computes a version of that topology in a lower dimensional space.

UMAP was developed under the belief that local structure is more important than global structure. It learns structures in a data set, even when the local structures can only be attributed to noise. It is not suitable for use in small, noisy data sets or in large data sets with only global (not local) structure. Figures produced using UMAP-reduced data should be interpreted with care: they could contain spurious structures from the data sample and not the target population. Additionally, UMAP is similar to t-SNE in that the dimensions produced by UMAP were generated nonlinearly and contain no true meaning.

We performed a preliminary comparison of PCA, t-SNE, and UMAP for visualizing high dimensional data using TensorFlow's Projector tool [TFP,]. This tool is a web interface for visualizing high dimensional data from either built-in data sets or data sets uploaded by the user. It supports all three of the dimensionality reduction methods discussed previously in this section as well as a customizable projection of the entire data set to two or three feature vectors. The PCA, t-SNE, and UMAP visualizations of the popular MNIST handwriting data set can be seen in Figure 10.

5.3 PREDICTING PATIENT OUTCOMES USING MOTION PATTERNS

In addition to examining the patterns of patient motion using unsupervised machine learning techniques, these patterns will also be used with supervised machine learning techniques to determine the relationship between motion types and clinical outcomes. In this section, we first present several supervised machine learning methods and then discuss more generally the limitations of supervised machine learning and the metrics we will use to evaluate our models.

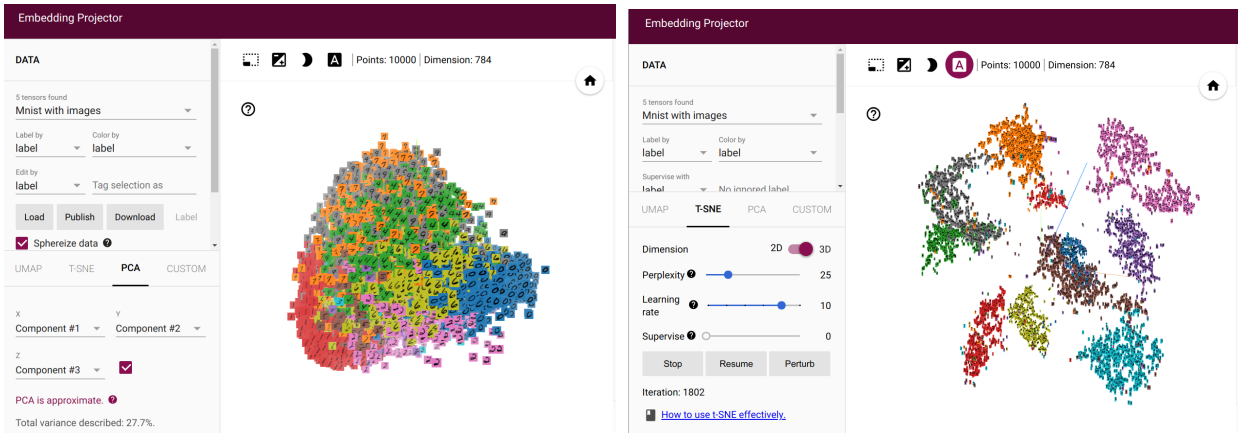

(a) PCA

(b) t-SNE

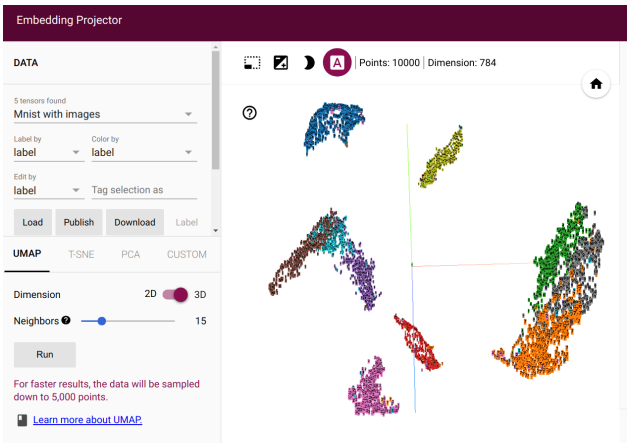

(c) UMAP

Figure 10: Visualization of MNIST data in 3D via TensorFlow Projector as generated using PCA, t-SNE, and UMAP dimensionality reduction techniques.

5.3.1 Regression

The first supervised machine learning method we discuss is regression. In general, regression maps a set of features to a set of outcomes. Each feature is weighted based on its contribution to the outcome. Features which are more relevant to the outcome have larger weights, while less important features have smaller weights.

The simplest version of regression is linear regression. Linear regression is used when the outcome being predicted has continuous values: a common example would be using the size of a house to predict its cost. The cost, y, would be modeled as

$$y = w_0 + w * x \tag{5.10}$$

where w is the weight assigned to the feature x, which is the size of the house, and w_0 is the weight for the bias in the model. As more features are added to the model, this equation generalizes to

$$y = w_0 + \sum_{i \in N} w_i * x_i \tag{5.11}$$

where w_i is the weight for feature i, x_i in the set of N features.

Alternatively, if the goal was to predict whether a house was owned or rented, linear regression would be a poor model choice. The goal of this problem is to identify a nominal class, not a value in a continuous interval. This type of problem is better suited for logistic regression.

Logistic regression takes the equation for linear regression and passes it through the logistic function to map it to a range of $[0, 1]$. The logistic function is

$$f(\pi) = \frac{1}{1 + e^{\pi}} \tag{5.12}$$

which means that a logistic regression models takes the form

$$y = \frac{1}{1 + e^{(w_0 + \sum_{i \in N} w_i * x_i)}} \tag{5.13}$$

This form of a logistic regression model is for binary, nominal outcomes, though multinomial logistic regression can model three or more outcomes and ordinal logistic regression can

model ordered, discrete outcomes. For the purposes of this document, when we say logistic regression, we mean the form which models binary, nominal outcomes.

The greatest strength and weakness of regression models is that they model linear relationships well. Linear models are fairly interpretable: the weights assigned to each feature in the linear model shows the importance the model believes that feature is. Interpretability is an important aspect of machine learning because people are more likely to trust a model if they can understand how it reached its conclusions. Unfortunately, it does not matter how interpretable the model is if the model is ill-suited for the data set. In particular, regression may have difficulty fitting data with nonlinear relationships.

5.3.2 Support Vector Machine

The mathematical framework for support vector machines (SVMs) was developed in 1963. In its original form, it could only be used to classify linearly separable data. SVMs treat data samples with n features as points in n-dimensional space. The SVM is composed of a collection of binary hyperplane classifiers. Binary hyperplane classifiers label data as belonging to a class or not belonging to that class depending on which side of the hyperplane the data is located. For a single binary hyperplane, the ideal location and alignment of the hyperplane is calculated using the following equation

$$\vec{w} \cdot \vec{x} + b = 0 \tag{5.14}$$

where $\vec{w}$ is the vector of weights assigned to the features in $\vec{x}$ and the variable b is a bias factor. This equation defines the hyperplane itself, but there are many hyperplanes that could satisfy this equation. The optimal hyperplane is determined using the support vectors.

The support vectors are the data points closest to the hyperplane. They define the location and orientation of the hyperplane. The space between the points on opposite sides of the hyperplane is called the margin, d. The optimal hyperplane is defined as the hyperplane whose $\vec{w}$ and b result in the largest d.

The largest d occurs when the weights for the data samples are minimized. The weights indicate how important a data sample is in defining the hyperplane. Data samples which

do not increase the size of d (are not support vectors) should not contribute to the model. These samples should be assigned weights of 0.

When the ideal $\vec{w}$ and b parameters have been determined, data on one side of the hyperplane is labeled as belonging to one class while the data on the other side of the hyperplane does not belong to that class. In a two class scenario, data that does not belong to one class clearly must belong to the other class. As more classes are added to a data set, the number of hyperplanes must also increase. Instead of optimizing a single hyperplane, the entire collection of hyperplanes must be optimized together.

In some cases, data with n dimensions may not be separable in n-dimensional space. In 1992, it was proposed that the original data could be mapped to a higher dimensional space where it would be linearly separable. The SVM could be built in that space and would still function as a linear classifier, even though it would appear to be a nonlinear classifier in the original space. Different kernel functions have been developed.

After a SVM model has been trained, the kernel used to map the data from n-dimensional space to the higher dimensional space is used to map new data to that space. The new data is assigned labels depending on where it lies in the higher dimensional space.

SVMs are versatile supervised learning techniques that perform well in classifying both linearly and nonlinearly separable data. By their very nature, they find the globally optimal solution. However, finding the optimal parameters for a SVM model can be a computationally expensive and complex process depending on the characteristics of the data samples.

5.3.3 LSTM Recurrent Neural Network

One of the most popular supervised learning algorithms is the artificial neural network. A basic artificial neural network is composed of connected layers of units modeled after neurons in a biological brain. Every artificial neural network has at least two layers: an input layer and an output layer. The number of neurons in the input layer is the same as the number of features in the data being fed to the network. The input layer is connected to the output layer by weighted edges. For a network with n features in the input layer and one neuron in

the output layer, the value predicted by the network for data point $\vec{x}$ is given as

$$f(\vec{x}) = \vec{w} \cdot \vec{x} + b \tag{5.15}$$

where $\vec{w}$ is the weight assigned to the edge connecting each input neuron to the output neuron, $\vec{x}$ is the values of the input vector, and b is an offset factor.

Layers can be added between the input layer and the output layer to model more complex relationships. These layers are called hidden layers because they are not seen at the data input or model output. The value of each neuron in each layer can be calculated using the values of the neurons in the previous layer, which means that for two layers, Equation 5.15 expands to

$$f(\vec{x}) = \vec{w_2}(\vec{w_1} \cdot \vec{x} + b_1) + b_2 \tag{5.16}$$

More generally, Equation 5.15 can be written as

$$f_n(\vec{x}) = \vec{w_n} f_{n-1}(\vec{x}) + b_n \tag{5.17}$$

where the dot product of the weights of the current layer w_n and the output $f_{n-1}(\vec{x})$ of the previous hidden layer $n-1$ are offset by some bias factor b_n to produce the output $f_n(\vec{x})$ of the current layer. For the first layer of the network, the output is calculated using Equation 5.15.

To model nonlinear relationships in data, this equation must be generalized further to allow for activation functions. Activation functions are intended to represent the action potential firing in a biological neuron. A biological neuron is either activated or not activated, but the activation function of a neuron in an artificial neural network is not limited to binary states. For example, the output of a rectified linear unit (ReLU) is in the range $[0, \text{inf})$, a sigmoid function's output is in the range $(0, 1)$, and a hyperbolic tangent produces a value in the range $(-1, 1)$. Different activation functions are used for different application depending on the desired behavior of the model.

We represent the activation function generically as $g_n(\cdot)$ and rewrite Equation 5.17 as

$$f_n(\vec{x}) = g_c\left(\vec{w_n} f_{n-1}(\vec{x}) + b_n\right) \tag{5.18}$$

Until this point, we have been describing feed-forward neural networks. All of the connections flow in a single direction from the input nodes to the output nodes. Networks built using a feed-forward paradigm are often used for pattern recognition or other cases where a given input is associated with a known output. However, neural networks can also have connections that skip layers, link back to previous layers, or connect to other neurons in the same layer. This type of network is called a recurrent neural network.

One particularly interesting type of recurrent neural network is a long short-term memory (LSTM) network. LSTM networks have more complex unit structure than basic neural networks. LSTM units are composed of a memory component and three types of gates: an input gate, an output gate, and a forget gate. The memory component tracks the current value of the unit. The input gate dictates how much data being passed to the cell impacts the memory component, the forget gate dictates how long a value is stored in the memory component, and the output gate dictates the impact of the value in the memory component is used to produce the output activation of the unit. Due to the nature of the LSTM units, networks made of LSTM units have an advantage over feed-forward networks when working with time-series data.

One of the major drawbacks of both regression and SVMs is that the data used to train these models must be in feature vector form. Neural networks have the ability to work with more complex input data. They have been used for tasks as complex as speech recognition and video processing using the audio or video itself as input. Their ability to work with data directly is a key strength of this type of technique. However, sequential data requires more memory than feature vectors. Similarly, the structure of artificial neurons needed to process and learn from these sequences is more complex and computationally expensive than regression, SVMs, or smaller and simpler neural network structures.

5.3.4 Application of Supervised Machine Learning

Generally, the outcomes of interest when applying supervised machine learning to medical data are some definition of normal and abnormal. We choose to perform two different analyses bases on two definitions of normal.

The first definition of normal is that enough motion can be removed from the image that the image is usable. The abnormal label is that the image cannot be recovered based on the patient's motion patterns.

The second definition of normal is that the patient is functioning typically. We choose to identify the opposite of this label as "the patient **may** not be functioning typically" because of the heterogeneity of our data. CHD is a heterogeneous disease with many presentation types, and the neurodevelopmental disorders add another degree of granularity and complexity to a subject's clinical diagnosis. While it would be impressive to be able to build a clinical decision support tool that can diagnose a patient as having a particular form of CHD accompanied by a specific neurocognitive disorder, this goal is not the purpose of this project.

If a machine learning model reaches 100% accuracy on both training and test data sets, data scientists should immediately assume something has gone wrong either with the model itself or with the training and testing data. Current machine learning models suffer from the difficulty of balancing two sources of error: bias and variance. Bias is the degree to which the machine learning model matches the underlying model of the training data. Variance is the breadth of the distribution of the data from the population of interest covered by the training data. Models with low bias and high variance overfit the training data: they model the training data well but generalize poorly to new data. Conversely, models with high bias and low variance underfit the training data: they fit the training data poorly, possibly because they learned noise in the training data rather than the signal. Underfitted models fail to capture the important signals from the training data and perform poorly overall.

A good model neither overfits nor underfits the training data. It has low bias and low variance, and the challenge of balancing these two sources of error has been discussed elsewhere but is important to address here to set realistic expectations about the training and testing classifications of a model. Ideally, the model will classify both training and

Table 1: An example of a truth table for a binary classifier predicting the presence or absence of a condition.

		Actual	
		Condition True	**Condition False**
Predicted	**Condition True**	True Positive (TP)	False Positive (FP)
	Condition False	False Negative (FN)	True Negative (TN)

testing data well, but it is not possible with current techniques and data availability for a model to have perfect classification of every data sample.

The "wellness"/"goodness" of a binary classification model is determined using a truth table. A truth table is a $2 * 2$ table filled with the number of occurrences where data was classified correctly and incorrectly as belonging to each class. An example table can be seen in Table 1.

Various metrics can be calculated from the truth table, such as sensitivity and precision. Sensitivity measures how well the model performed at correctly identifying actually true data samples:

$$sensitivity = TPR = \frac{TP}{TP + FN} \tag{5.19}$$

Precision measures the ratio of positive predictions to actually true data:

$$specificity = PPV = \frac{TP}{TP + FP} \tag{5.20}$$

These metrics are also known as the true positive rate and the positive predictive value, respectively.

These metrics are independently informative about different aspects of the model, but during training only one metric is used to evaluate a model's performance. Accuracy, for

example, is a measure of how many data samples were classified correctly:

$$A = \frac{TP + TN}{TP + TN + FP + FN} \tag{5.21}$$

We choose to use the balanced F1 score to evaluate the success of our supervised learning models. The balanced F1 score is calculated as:

$$\begin{aligned} F1 &= \frac{2 \cdot TPR \cdot PPV}{TPR + PPV} \\ &= \frac{2 \cdot TP}{2 \cdot TP + FP + FN} \end{aligned} \tag{5.22}$$

The balanced F1 score places equal value on a model correctly identifying actually true data compared to false data as well as identifying as much actually true data as possible. Accuracy only accounts for the number of correctly classified data samples. In cases where all classes in a data set are not evenly represented, the balanced F1 score produces a more robust model than accuracy.

5.4 DESCRIBING MOTION PATTERNS

In previous sections we describe practical knowledge about how fetal, neonatal, preadolescent, and adult patients move in different ways during MRI scans. We wish to quantify these movement patterns using the metrics described earlier in this chapter and identify appropriate terminology that can be used to describe them.

6.0 DATA

The data used to test the hypothesis and aims introduced in the previous chapter are drawn from several subject populations. Because motion causes problems in MR images across all stages of life, we used images from cohorts of healthy and CHD fetal, neonatal, preadolescent, and adult subjects gathered in as part of ongoing studies. Data from these studies was obtained through studies approved by the IRB at the Children's Hospital of Pittsburgh of UPMC and the University of Pittsburgh. The data is stored and accessed in compliance with all HIPPA policies.

We use data from a simulated phantom as well as healthy adult human phantoms. The healthy adult human phantom data collection was also approved by the IRB at the Children's Hospital of Pittsburgh of UPMC and the University of Pittsburgh and is stored and accessed in compliance with all HIPPA policies.

The final data set we use is from the Alzheimer's Disease Neuroimaging Initiative (ADNI) database (adni.loni.usc.edu). The ADNI was launched in 2003 as a public-private partnership, led by Principal Investigator Michael W. Weiner, MD. The primary goal of ADNI has been to test whether serial magnetic resonance imaging (MRI), positron emission tomography (PET), other biological markers, and clinical and neuropsychological assessment can be combined to measure the progression of mild cognitive impairment (MCI) and early Alzheimer's disease (AD). For up-to-date information, see www.adni-info.org.

6.1 NEONATAL SUBJECT POPULATION AND IMAGES

Neonatal subjects are recruited as part of a prospective observational study. The subjects were scanned using a 3T Skyra (Siemans AG, Erlangen, Germany). They were unsedated during the scans and a "feed and bundle" protocol was used to prevent motion during the scans [Windram et al., 2011]. The newborns were positioned in the coil to minimize head tilting. Newborns were fitted with earplugs (Quiet Earplugs; Sperian Hearing Protection, San Diego, CA) and neonatal ear muffs (MiniMuffs; Natus, San Carlos, CA). An MR-compatible vital signs monitoring system (Veris, MEDRAD, Inc. Indianola, PA) was used to monitor neonatal vital signs. All scans were performed using a multi-channel head coil. The parameters for the resting-state BOLD MR scans were FOV=240 mm and TE/TR=32/2020 ms with interplane resolution of 4x4 mm, slice thickness of 4 mm, and 4 mm space between slices. The acquired images contained 150 volumes where each volume consisted of 64x64x32 voxels^3.

6.2 PREADOLESCENT SUBJECT POPULATION AND IMAGES

As part of a multicenter study of CHD in preadolescents, we collected rs-fMRIs from nine sites throughout the United States. These images were of patients in the age range of 9 to 13 years who either had CHD or were healthy with no neurocognitive impairments. In addition to the MRI scans, subjects who participated in this study were asked to participate in additional testing either to determine their neurocognitive outcome status or to perform genetic analyses.

6.3 ADULT SUBJECT POPULATION AND IMAGES

As the prognosis for patients with CHD improves, their life expectancy also increases. The aging CHD population presents new questions about the connection between CHD and

neurocognitive challenges associated with aging. As patients age, there is an expectation that their images will contain less motion for a time. If a patient begins to show signs of cognitive impairment due to aging, it can be expected that their images will begin to contain more motion as their neurocognitive state deteriorates.

We include a cohort of adult subjects over a wide range of ages in our study. The purpose of using images from this cohort is to demonstrate the generalizability of the DAG-based framework to adult patients as well as its use in different clinical populations. This cohort is being studied as part of an ongoing, prospective study of CHD and neurodevelopment. The data collected for these subject includes rs-fMRIs, behavioral, and clinical data from healthy and CHD adult subjects.

6.4 FETAL SUBJECT POPULATION AND IMAGES

Fetal subjects have different constraints on their physical environment than neonates, preadolescents, and adults. As a result, they exhibit unique patterns of motion. The previous subject cohorts discussed in this chapter have the following commonalities: the subject experiences the full effects of gravity, the subject is lying on his back in an MRI scanner, and the subject's head motion is limited by the head coil within the MRI. Any motion in these images is a direct result of the subject himself moving, whether passively (cardiac motion and breathing) or actively (fidgeting or looking around).

A fetal subject is scanned in vivo. He is suspended in amniotic fluid within his mother. The amniotic fluid has buoyancy that reduces the effects of gravity and allows a fetal subject significant freedom of movement. The fetus can rotate, shift, and flip in ways that can only be accomplished when floating in a body of water. The properties of the uterus constrain the physical space in which a motion could occur, but not as much as the head coil and gravity do to the other patient cohorts. A fetus is not guaranteed to be in any specific position at the start of the scan: the scan begins when the mother is ready, not when the fetus achieves a certain pose.

The fetal subjects underwent fetal echocardiography scans in a cardiac clinic to determine

whether they were healthy or had a form of CHD. They were then scanned on an MRI scanner. Images of the fetal brain and the placenta were acquired for each subject.

We are interested in both the fetal brain and placental images for our work because of the relationship between placenta and brain development. However, these organs have very different physical properties. The fetal brain is a rigid structure floating and moving within the amneotic fluid. It undergoes translation and rotation as a single unit due to passive and active maternal and fetal motions. The placenta, on the other hand, is anchored in place on the uterine wall. It may undergo small translations or rotations due to maternal motion, but it will respond differently to fetal motion. Fetal motions cause nonlinear deformations of the pliable placenta that can only be adequately accounted for using nonlinear registration algorithms. Nonlinear registrations have the potential to deform brain images into physically impossible shapes, so the fetal brain and placenta were manually segmented in their respective images so that each organ could undergo independent motion correction.

The segmenters were one of a group of four researchers. While one researcher trained the other three group members, the interrater agreement between them is still being determined.

6.5 SIMULATED PHANTOM IMAGES

Every MRI scanner is different, so a stand-in model for an organ or tissue type is often used to calibrate an MRI scanner. The model is designed to have specific physical properties which mimic the physical properties of the organ or tissue. These properties can be accurately measured during the design process of this model so that the radiologist or researcher looking at images of the model can know the ground truth of the model. Because these models mimic true organs and tissues, they are called phantoms.

We will generate a simulated phantom image using the rs-fMRI of a healthy adult male. A single volume will be selected from the rs-fMRI sequence. This volume will be duplicated to create a generated image with 150 instances of the same volume. This sequence will be our base phantom sequence.

A copy of the base phantom sequence will be made and a subvolume in the same location

of every volume will be selected. In the subvolume of each frame, a small amount of noise generated using a normal Gaussian distribution will be added to simulate changes in blood oxygen level-dependent signal over time. The noise will be generated from a normal Gaussian distribution will be added to each frame. This image sequence will be referred to as our BOLD phantom sequence.

6.6 HUMAN PHANTOM IMAGES

One of the major challenges in the medical imaging field is collecting a large enough set of data with a high enough quality to generate statistically significant results. As part of a multisite study, a set of five healthy adult male subjects were scanned at several different sites within a period of ten weeks.

These subjects are considered human phantoms because of their health adult status, but they still may contain some motion. Their images are included in this study so that we can determine the consistency and effects of the motion correction pipeline on images of the same subject at different points in time.

6.7 PURPOSE FOR EACH COHORT

6.7.1 Simulated Phantom

The phantom experiments will be used to probe the volume registration technique. By applying the DAG-based and traditional registration techniques to the base phantom sequence, we will be able to evaluate the degrees of positional and signal change errors each technique may introduce into the registration process. After determining the baseline error, we will apply both registration techniques to the BOLD phantom sequence. The registered versions of the BOLD phantom sequence will be compared to each other and to the original BOLD phantom sequence to determine how well each registration retains the BOLD signal.

This particular experiment will be one of the first to investigate how much true BOLD signal is preserved through motion correction. One of the major drawbacks to existing motion correction pipelines is that they remove signal along with noise. In clinical data, there is no way to know the ground truth signal contained within the image; however, simulated phantom images have a de facto known ground truth signal. The design for this experiment can be used to evaluate how much BOLD signal is recovered by other motion correction pipelines, and how close the recovered signal is to the signal of interest.

6.7.2 Human Phantom

The human phantom images from all sites will be used both as a set of true healthy control adults and as examples of low motion images of the same subjects taken at multiple sites.

6.7.3 Clinical Images

Neonatal Cohort. Our set of neonatal subjects includes a cohort of 74 healthy neonates. Each subject in this cohort underwent an MRI scan, and the rs-fMRIs obtained during this process were compared to Power et al.'s positional and signal change usability thresholds. Of the 74 subjects, 17 of them had rs-fMRIs which did not meet the usability criteria. These high motion images were used to test the feasibility of the DAG-based volume registration framework.

These images were ideal for the feasibility study for three reasons. First, the neonates were healthy, which eliminates disease status as a confounding variable in the analysis of the registered images. Second, the neonates in this study were scanned using a feed and sleep protocol. Because the neonates were asleep during the scan, they generally did not move very much. The high-motion neonates are an obvious exception to this concept, but many of the high-motion images contained long periods where the subject was stationary. Evaluating the DAG-based framework on data with various patterns of motion and different periods of low and high motion allowed us to explore the effects of the DAG-based algorithm in different combinations of motion features. Third, these images were too corrupted by motion to be used in other analyses. Applying both the DAG-based framework and the

traditional registration framework to these images provided the opportunity to compare the performances of both registration frameworks to each other in the context of the usability gold standard thresholds.

Preadolescent Cohort. The multicenter imaging study of preadolescent subjects provides a unique opportunity to evaluate the efficacy of the DAG-based framework on a large subject cohort containing variable amounts of motion. The outcome of this experiment will be used in the next experiment to determine if there are any site-specific or vendor-specific variables influencing patient motion.

Adult Cohorts. The adult cohorts encompass many clinical outcomes and a wider age range than the other clinical populations.

Fetal Cohort. As the fetal subjects have both neurological and placental images, their data will be used to examine the impact of volume registration on different organ types.

7.0 PRELIMINARY RESULTS

7.1 COMPARISON OF VOLUME REGISTRATION METHODS

7.1.1 Subject Position Variability in the Registered Images

Each rs-fMRI sequence in the cohort underwent registration using both frameworks. For each sequence, the correlation ratio between every possible pair of volumes was calculated. A set of metrics of the correlation ratio matrices for each sequence can be seen in Table 2. This table shows that the original sequences generally have higher average correlation ratios and contain more variation in their correlation ratios than the globally registered images. The registration methods were able to reduce the mean and variability of the correlation ratios across all subjects in the cohort who had original correlation ratio averages of at least 0.035.

7.1.2 Comparison of Motion Correction Methods

The FD and DVARS values were calculated to determine how many volumes in each registered sequence met the FD and DVARS thresholds. The FD and DVARS values also considered to be distribution functions representing the effects of no registration, traditional registration, and DAG-based registration. These distributions were compared using the Kolmogorov-Smirnov test, which compares the empirical distribution functions of two samples. There were statistically significant differences between the FD and DVARS values of all sequences at $p < 2.2 * 10^{-16}$. Statistics calculated for the FD and DVARS value histograms of both motion correction methods can be seen in Table 3.

Power et al.'s usability thresholds were used to determine how many volumes were recov-

ered by each framework [Power et al., 2014]. Table 4 shows the number of volumes meeting each threshold, with the traditional and DAG-based frameworks recovering 2% and 10% of volumes, respectively. These results show that the DAG-based registration technique produces sequences with lower FD and DVARS value than the traditional global registration method does.

Table 2: The mean and standard deviation for each sequences correlation ratio matrix for every subject.

	Original Sequence		**Traditional Registration**		**DAG-based Registration**	
Subject	**Mean**	**Standard Deviation**	**Mean**	**Standard Deviation**	**Mean**	**Standard Deviation**
0	0.04476	0.02707	0.03842	0.01167	0.03194	0.01082
1	0.04339	0.02926	0.03323	0.00771	0.03903	0.01315
2	0.03464	0.01773	0.04522	0.01359	0.03768	0.00775
3	0.03431	0.00264	0.03203	0.01097	0.03528	0.00289
4	0.03288	0.00462	0.02601	0.00981	0.03364	0.00514
5	0.03234	0.01376	0.02986	0.00958	0.03390	0.00800
6	0.03145	0.00730	0.02691	0.00685	0.03065	0.00496
7	0.02970	0.03314	0.03331	0.00736	0.03025	0.00969
8	0.02728	0.01044	0.03060	0.00500	0.03359	0.00791
9	0.02467	0.00305	0.03354	0.00513	0.02467	0.00303
10	0.02446	0.00163	0.03535	0.00293	0.02446	0.00163
11	0.02422	0.01161	0.02958	0.00559	0.02617	0.00981
12	0.02338	0.00060	0.02467	0.00304	0.02338	0.00060
13	0.02280	0.00101	0.02447	0.00163	0.02279	0.00101
14	0.01968	0.01040	0.02338	0.00060	0.02740	0.00664
15	0.01942	0.00526	0.02279	0.00101	0.02939	0.00548
16	0.01414	0.00133	0.01512	0.00178	0.01520	0.00184

Table 3: The mean, median, standard deviation, skewness, and kurtosis of the histograms of FD and DVARS values for all image types were calculated. The histograms for the DAG-based method have lower means, medians, and standard deviations than those of the first volume correction method.

	FD Values (mm)			**DVARS Values (units)**		
Statistic	**None**	**Traditional**	**DAG-based**	**None**	**Traditional**	**DAG-based**
Mean	1.07	2.18	1.22	63.14	135.15	97.23
Median	0.30	1.46	0.56	35.19	133.48	77.75
Standard Deviation	1.97	2.35	1.61	70.00	83.48	77.14
Skewness (-)	3.86	3.08	3.00	2.76	1.13	1.55
Kurtosis (-)	23.29	17.74	17.12	14.28	7.79	7.44

Table 4: The number of frames recovered by each global volume registration framework for each threshold.

Threshold	**None**	**Traditional**	**DAG-based**
FD (0.2 mm)	966	175	569
DVARS (25 units)	781	78	297
Both	619	61	258
Both (%)	24.27%	2.39%	10.11%

8.0 DISCUSSION

8.1 COMPARISON OF VOLUME REGISTRATION METHODS

Resting-state BOLD MR images are used to evaluate the functional architecture of a patient's brain. Because resting-state BOLD images are highly susceptible to motion, development of strong post-acquisition motion correction techniques is vital. Current pipelines for mitigating motion after sequence acquisition vary in terms of efficacy and effectiveness, but all begin with global volume registration. In this study, we compared the corrective performance of two global volume registration methods, the traditional framework and a novel DAG-based framework, on a set of 17 neonatal rs-fMRIs.

The correlation ratio matrices, FD, and DVARS values were calculated for each sequence. The decrease in the mean and standard deviations of the correlation ratio matrices for the registered sequences indicate that global volume registration reduces some effects of motion in rs-fMRIs. The histograms of the FD and DVARS values in the registered sequences show that the DAG-based method was better able to correct volumes to meet Power et als thresholds than the traditional registration method. These results indicate that the DAG-based global registration method is better able to reduce the effects of motion than the traditional global registration method when correcting motion in neonatal images. While no entire sequences were recovered, some high-motion volumes within each sequence were recovered by the DAG-based registration method that were not recovered by the traditional registration method.

8.1.1 Relation to Existing Work

To the best of our knowledge, the only other study that has used a variant of the DAG-based method was performed by Liao et al [Liao et al., 2016]. Liao et als dataset consisted of 10 fetal rs-fMRIs. In each of these sequences, the fetal brain, fetal liver, and placenta were manually segmented in the first volume of the sequence as well as in five other randomly chosen volumes. These overlap of these manual segmentations before and after registration as measured using the Dice coefficient was used to quantify the amount of motion in each sequence. Even though the Dice coefficients increase more in each sequence after Liao et al.s registration than after traditional registration, their measure of positional change fails to quantify any changes in position between any other pairs of volumes that do not have manual segmentations.

8.1.2 Limitations and Future Work

Subject motion during rs-MRI scans affects both the recorded position and orientation of the subject as well as the established magnetic spin gradients within the skull. The DAG-based technique can correct the positional effects of motion, but it cannot correct the effects of the motion that disrupt the magnetic spin gradients. Methods for prospectively estimating subject motion exist and can be used to change slice positions in each volume during acquisition. Retrospective techniques to correct for this effect will require shot-to-shot modeling of macroscopic B_0 fields and are beyond the scope of the present research.

In the future, we plan to apply the DAG-based technique to a cohort of preadolescent images for the purpose of characterizing motion in a large cohort as well as to a cohort of neonatal images to address the problem of correcting motion of multiple organs in images with large amounts of motion.

8.1.3 Conclusions

In this feasibility study, we applied two global registration methods to set of rs-fMRIs of 17 healthy neonates. We showed that both global registration techniques reduce the amount

of motion in the images as measured using the correlation ratio. We then showed that the DAG-based framework is better at correcting images to a pair of established gold standard thresholds for resting-state BOLD MRI usability than the traditional framework. In the future we plan to apply the DAG-based framework to other patient populations and multi-organ problems.

9.0 CONCLUSIONS

This is the second chapter of the present dissertation. It is more interesting than the first one, for it is the last one.

APPENDIX

VOLUME REGISTRATION PARAMETERS

The parameters used for the registration of pairs of image volumes can be seen below.

```
##
# Register a pair of image volumes
#
# Effects: save a copy of the registered image and the registration
    ↪ parameters
#
# @param fixedImgFn The filename of the fixed image as a string
# @param movinImgFn The filename of the moving image as a string
# @param regImgOutFn The filename as a string specifying where to save the
    ↪  registered moving image
# @param transformPrefix
# @param initialize Optional parameter to specify the location of the
    ↪ transform matrix from the previous registration
# @param regType Optional parameter to specify the type of registration to
    ↪  use (affine ['Affine'] or nonlinear ['Syn']) Default: nonlinear
def registerVolumes(fixedImgFn, movinImgFn, regImgOutFn, transformPrefix,
    ↪ initialize=None, regtype='nonlinear'):
```

```
# Registration set up: for both Affine and SyN transforms
reg = Registration()
reg.inputs.fixed_image = fixedImgFn
reg.inputs.moving_image = movinImgFn
reg.inputs.output_transform_prefix = transformPrefix
reg.inputs.interpolation = 'NearestNeighbor'
reg.inputs.dimension = 3
reg.inputs.write_composite_transform = False
reg.inputs.collapse_output_transforms = False
reg.inputs.initialize_transforms_per_stage = False
reg.inputs.num_threads = 100
reg.inputs.output_warped_image = regImgOutFn

# Registration set up: Specify certain parameters for the Affine
   ↪ registration step
reg.inputs.transforms = ['Affine']
reg.inputs.transform_parameters = [(2.0,)]
reg.inputs.number_of_iterations = [[1500, 200]]
reg.inputs.metric = ['CC']
reg.inputs.metric_weight = [1]
reg.inputs.radius_or_number_of_bins = [5]
reg.inputs.convergence_threshold = [1.e-8]
reg.inputs.convergence_window_size = [20]
reg.inputs.smoothing_sigmas = [[1,0]]
reg.inputs.sigma_units = ['vox']
reg.inputs.shrink_factors = [[2,1]]
reg.inputs.use_estimate_learning_rate_once = [True]
reg.inputs.use_histogram_matching = [True] # This is the default, but
   ↪ specify it anyway
```

```
# Registration set up: nonlinear transforms only
if regtype == 'nonlinear':
    reg.inputs.transforms.append('SyN')
    reg.inputs.transform_parameters.append((0.25, 3.0, 0.0))
    reg.inputs.number_of_iterations.append([100, 50, 30])
    reg.inputs.metric.append('CC')
    reg.inputs.metric_weight.append(1)
    reg.inputs.radius_or_number_of_bins.append(5)
    reg.inputs.convergence_threshold.append(1.e-9)
    reg.inputs.convergence_window_size.append(20)
    reg.inputs.smoothing_sigmas.append([2,1,0])
    reg.inputs.sigma_units.append('vox')
    reg.inputs.shrink_factors.append([3,2,1])
    reg.inputs.use_estimate_learning_rate_once.append(True)
    reg.inputs.use_histogram_matching.append(True) # This is the default
        ↪ value, but specify it anyway

# If the registration is initialized, set a few more parameters
if initialize is not None:
    reg.inputs.initial_moving_transform = initialize
    reg.inputs.invert_initial_moving_transform = False

# Keep the user updated with the status of the registration
print("Starting", regtype, "registration␣for", regImgOutFn)

# Run the registration
reg.run()

# Keep the user updated with the status of the registration
print("Finished", regtype, "registration␣for", regImgOutFn)
```

BIBLIOGRAPHY

[TFP,] TensorFlow Projector.

[Abdi and Williams, 2010] Abdi, H. and Williams, L. J. (2010). Principal component analysis. *WIREs Computational Statistics*, 2:433–459.

[Aksoy et al., 2008] Aksoy, M., Newbould, R., Straka, M., Holdsworth, S. J., Skare, S. T., Santos, J. M., and Bammer, R. (2008). A Real Time Optical Motion Correction System Using a Single Camera and 2D Marker. *Proceedings of the 16th Scientific Meeting of ISMRM*, 16:3120.

[Alexander, 2012] Alexander, M. (2012). Managing Patient Stress in Pediatric Radiology. *Radiologic Technology*, 83(6):549–560.

[Assaf et al., 2010] Assaf, M., Jagannathan, K., Calhoun, V. D., Miller, L., Stevens, M. C., Sahl, R., O'Boyle, J. G., Schultz, R. T., and Pearlson, G. D. (2010). Abnormal functional connectivity of default mode sub-networks in autism spectrum disorder patients. *NeuroImage*, 53(1):247–256.

[Avants et al., 2014] Avants, B. B., Tustison, N. J., Stauffer, M., Song, G., Wu, B., and Gee, J. C. (2014). The Insight ToolKit image registration framework. *Frontiers in Neuroinformatics*, 8(April).

[Ayres, 1920] Ayres, L. P. (1920). The correlation ratio. *The Journal of Educational Research*, 2(1):452–456.

[Barnea-Goraly et al., 2014] Barnea-Goraly, N., Weinzimer, S. A., Ruedy, K. J., Mauras, N., Beck, R. W., Marzelli, M. J., Mazaika, P. K., Aye, T., White, N. H., Tsalikian, E., Fox, L., Kollman, C., Cheng, P., and Reiss, A. L. (2014). High success rates of sedation-free brain MRI scanning in young children using simple subject preparation protocols with and without a commercial mock scanner - the Diabetes Research in Children Network (DirecNet) experience. *Pediatric Radiology*, 44(2):181–186.

[Beckmann et al.,] Beckmann, C. F., Deluca, M., Devlin, J. T., and Smith, S. M. Investigations into Resting-state Connectivity using Independent Component Analysis (FMRIB Technical Report TR05CB1).

[Beckmann and Smith, 2004] Beckmann, C. F. and Smith, S. M. (2004). Probabilistic Independent Component Analysis for Functional Magnetic Resonance Imaging. *IEEE Transactions on Medical Imaging*, 23(2):137–152.

[Behzadi et al., 2007] Behzadi, Y., Restom, K., Liau, J., and Liu, T. T. (2007). A component based noise correction method (CompCor) for BOLD and perfusion based fMRI. *NeuroImage*, 37(1):90–101.

[Bharatha et al., 2001] Bharatha, A., Hirose, M., Hata, N., Warfield, S. K., Ferrant, M., Zou, K. H., Suarez-Santana, E., Ruiz-Alzola, J., D'Amico, A., Cormack, R. A., Kikinis, R., Jolesz, F. A., and Tempany, C. M. (2001). Evaluation of three-dimensional finite element-based deformable registration of pre- and intraoperative prostate imaging. *Medical Physics*, 28(12):2551–60.

[Coté and Wilson, 2016] Coté, C. J. and Wilson, S. (2016). Guidelines for Monitoring and Management of Pediatric Patients Before, During, and After Sedation for Diagnostic and Therapeutic Procedures: Update 2016. *Pediatrics*.

[Dewey et al., 2007] Dewey, M., Schink, T., and Dewey, C. F. (2007). Claustrophobia during magnetic resonance imaging: Cohort study in over 55,000 patients. *Journal of Magnetic Resonance Imaging*, 26(5):1322–1327.

[Dice, 1945] Dice, L. R. (1945). Measures of the Amount of Ecologic Association Between Species. *Ecology*, 26(3):297–302.

[Dosenbach et al., 2017] Dosenbach, N. U., Koller, J. M., Earl, E. A., Miranda-Dominguez, O., Klein, R. L., Van, A. N., Snyder, A. Z., Nagel, B. J., Nigg, J. T., Nguyen, A. L., Wesevich, V., Greene, D. J., and Fair, D. A. (2017). Real-time motion analytics during brain MRI improve data quality and reduce costs. *NeuroImage*, 161(January):80–93.

[Forman et al., 2011] Forman, C., Aksoy, M., Hornegger, J., and Bammer, R. (2011). Self-encoded marker for optical prospective head motion correction in MRI. *Medical Image Analysis*, 15(5):708–719.

[Fox et al., 2015] Fox, C. K., Sidney, S., and Fullerton, H. J. (2015). Community-based case–control study of childhood stroke risk associated with congenital heart disease. *Stroke*, 46(2):336–340.

[Friston et al., 1995] Friston, K. J., Ashburner, J., Frith, C. D., Poline, J. ., Heather, J. D., and Frackowiak, R. S. (1995). Spatial registration and normalization of images. *Human Brain Mapping*, 3(3):165–189.

[Friston et al., 1996] Friston, K. J., Williams, S., Howard, R., Frackowiak, R. S. J., and Turner, R. (1996). Movement-Related effects in fMRI time-series. *Magnetic Resonance in Medicine*, 35(3):346–355.

[Gale et al., 2013] Gale, C., Jeffries, S., Logan, K. M., Chappell, K. E., Uthaya, S. N., and Modi, N. (2013). Avoiding sedation in research MRI and spectroscopy in infants: our approach, success rate and prevalence of incidental finding. *Arch Dis Child Fetal Neonatal Ed*, 98:F267–F268.

[Garcia-Palacios et al., 2007] Garcia-Palacios, A., Hoffman, H. G., Richards, T. R., Seibel, E. J., and Sharar, S. R. (2007). Use of Virtual Reality Distraction to Reduce Claustrophobia Symptoms during a Mock Magnetic Resonance Imaging Brain Scan: A Case Report. *CyberPsychology and Behavior*, 10(3):485–488.

[Giang et al., 2018] Giang, K. W., Mandalenakis, Z., Dellborg, M., Lappas, G., Eriksson, P., Hansson, P.-O., and Rosengren, A. (2018). Long-Term Risk of Hemorrhagic Stroke in Young Patients With Congenital Heart Disease. *Stroke*, pages 1155–1162.

[Gorgolewski et al., 2011] Gorgolewski, K., Burns, C. D., Madison, C., Clark, D., Halchenko, Y. O., Waskom, M. L., and Ghosh, S. S. (2011). Nipype : a flexible , lightweight and extensible neuroimaging data processing framework in Python. *Frontiers in Neuroinformatics*, 5(August).

[Greicius et al., 2003] Greicius, M. D., Krasnow, B., Reiss, A. L., and Menon, V. (2003). Functional connectivity in the resting brain: A network analysis of the default mode hypothesis. *Proceedings of the National Academy of Sciences of the United States of America*, 100(1):253–258.

[Harned and Strain, 2001] Harned, R. K. and Strain, J. D. (2001). MRI-compatible audio / visual system : impact on pediatric sedation. *Pediatric Radiology*, pages 247–250.

[Hartigan and Wong, 1979] Hartigan, J. A. and Wong, M. A. (1979). Algorithm AS 136 A K-Means Clustering Algorithm. *Journal of the Royal Statistical Society*, 28(1):100–108.

[Jenkinson et al., 2002] Jenkinson, M., Bannister, P., Brady, M., and Smith, S. (2002). Improved Optimization for the Robust and Accurate Linear Registration and Motion Correction of Brain Images. *NeuroImage*, 17:825–841.

[Jenkinson and Smith, 2001] Jenkinson, M. and Smith, S. (2001). A global optimisation method for robust affine registration of brain images. *Medical Image Analysis*, 5:143–156.

[Jo et al., 2013] Jo, H. J., Gotts, S. J., Reynolds, R. C., Bandettini, P. A., Martin, A., Cox, R. W., and Saad, Z. S. (2013). Effective preprocessing procedures virtually eliminate distance-dependent motion artifacts in resting state FMRI. *Journal of Applied Mathematics*, 2013.

[Jo et al., 2010] Jo, H. J., Saad, Z. S., Simmons, W. K., Milbury, L. A., and Cox, R. W. (2010). Mapping sources of correlation in resting state FMRI, with artifact detection and removal. *NeuroImage*, 52(2):571–582.

[Juan and Vidal, 1998] Juan, A. and Vidal, E. (1998). Fast Median Search in Metric Spaces. In *Joint IAPR International Workshops on Statistical Techniques in Pattern Recognition (SPR) and Structural and Syntactic Pattern Recognition (SSPR)*, pages 905–912. Springer.

[Kaufman and Rousseeuw, 1987] Kaufman, L. and Rousseeuw, P. J. (1987). Clustering By Means Of Mediods. In *Statistical Data Analysis Based on the {\displaystyle L_{1}}Norm and Related Methods*, pages 405–416. North Holland/Elsevier, Amsterdam.

[Khalil et al., 1994] Khalil, A., Aggarwal, R., Thirupuram, S., and Arora, R. (1994). Incidence of Congenital Heart Disease Among Hospital Live Births in India. *Journal of Indian Pediatrics*, 31:519–527.

[Khan et al., 2007] Khan, J. J., Donnely, L. F., Koch, B. L., Curtwright, L. A., Dickerson, J. M., Hardin, J. L., Hutchinson, S., Wright, J., and Gessner, K. E. (2007). A program to decrease the need for pediatric sedation for CT and MRI. *Applied Radiology*, April:30–33.

[KinetiCor Biometric Intelligence, 2019] KinetiCor Biometric Intelligence (2019). The kineticor platform.

[Laumann et al., 2015] Laumann, T. O., Gordon, E. M., Adeyemo, B., Snyder, A. Z., Joo, S. J., Chen, M.-Y., Gilmore, A. W., McDermott, K. B., Nelson, S. M., Dosenbach, N. U., Schlaggar, B. L., Mumford, J. A., Poldrack, R. A., and Petersen, S. E. (2015). Functional System and Areal Organization of a Highly Sampled Individual Human Brain. *Neuron*, 87(3):657–670.

[Li, 1990] Li, W. (1990). Mutual Information Functions versus Correlation Functions. *Journal of Statistical Physics*, 60(5/6):823–837.

[Liao et al., 2005] Liao, R., Krolik, J. L., and McKeown, M. J. (2005). An information-theoretic criterion for intrasubject alignment of FMRI time series: Motion corrected independent component analysis. *IEEE Transactions on Medical Imaging*, 24(1):29–44.

[Liao et al., 2016] Liao, R., Turk, E. A., Zhang, M., Luo, J., Ellen Grant, P., Adalsteinsson, E., and Golland, P. (2016). Temporal registration in in-utero volumetric MRI time series. *Lecture Notes in Computer Science (including subseries Lecture Notes in Artificial Intelligence and Lecture Notes in Bioinformatics)*, 9902 LNCS:54–62.

[Maclaren et al., 2013] Maclaren, J., Herbst, M., Speck, O., and Zaitsev, M. (2013). Prospective motion correction in brain imaging: A review. *Magnetic Resonance in Medicine*, 69(3):621–636.

[MacQueen, 1967] MacQueen, J. (1967). Some methods for classification and analysis of multivariate observations. In *Proceedings of the fifth Berkeley symposium on mathematical statistics and probability*, volume 1, pages 281–297. Oakland, CA, USA.

[Malviya et al., 2000] Malviya, S., Voepel-Lewis, T., Prochaska, G., and Tait, A. R. (2000). Prolonged Recovery and Delayed Side Effects of Sedation for Diagnostic Imaging Studies in Children. *Pediatrics*, 105(3).

[Mathur et al., 2008] Mathur, A. M., Neil, J. J., McKinstry, R. C., and Inder, T. E. (2008). Transport, monitoring, and successful brain MR imaging in unsedated neonates. *Pediatric Radiology*, 38(3):260–264.

[McInnes et al., 2018] McInnes, L., Healy, J., and Melville, J. (2018). UMAP: Uniform Manifold Approximation and Projection for Dimension Reduction. *arXiv preprint arXiv:1802.03426*.

[Mebius et al., 2017] Mebius, M. J., Kooi, E. M., Bilardo, C. M., and Bos, A. F. (2017). Brain Injury and Neurodevelopmental Outcome in Congenital Heart Disease: A Systematic Review. *Pediatrics*, 140(1):e20164055.

[Mozaffarian et al., 2016] Mozaffarian, D., Benjamin, E. J., Go, A. S., Arnett, D. K., Blaha, M. J., Cushman, M., Das, S. R., Ferranti, S. D., Després, J.-p., Fullerton, H. J., Howard, V. J., Huffman, M. D., Isasi, C. R., Jiménez, M. C., Judd, S. E., Kissela, B. M., Lichtman, J. H., Lisabeth, L. D., Liu, S., Mackey, R. H., Magid, D. J., McGuire, D. K., Mohler, E. R., Moy, C. S., Muntner, P., Mussolino, M. E., Nasir, K., Neumar, R. W., Nichol, G., Palaniappan, L., Pandey, D. K., Reeves, M. J., Rodriguez, C. J., Rosamond, W., Sorlie, P. D., Stein, J., Towfighi, A., Turan, T. N., Virani, S. S., Woo, D., Yeh, R. W., and Turner, M. B. (2016). *Heart Disease and Stroke Statistics 2016 Update A Report From the American Heart Association*. American Heart Association.

[Murphy and Brunberg, 1997] Murphy, K. J. and Brunberg, J. A. (1997). Adult claustrophobia, anxiety and sedation in MRI. *Magnetic Resonance Imaging*, 15(1):51–54.

[Nadler and Galun, 2007] Nadler, B. and Galun, M. (2007). Fundamental limitations of spectral clustering. *Advances in Neural Information Processing Systems*, pages 1017–1024.

[Ng et al., 2002] Ng, A. Y., Jordan, M. I., and Weiss, Y. (2002). On spectral clustering: Analysis and an algorithm. In *Advances in neural information processing systems*, pages 849–856.

[Nikyar et al., 2011] Nikyar, B., Sedehi, M., Mirfazeli, A., Qorbani, M., and Golalipour, M.-J. (2011). Prevalence and Pattern of Congenital Heart Disease among Neonates in Gorgan, Northern Iran (2007-2008). *Iranian Journal of Pediatrics*, 21(3):307–12.

[Parkes et al., 2017] Parkes, L., Fulcher, B. D., Yucel, M., and Fornito, A. (2017). An evaluation of the efficacy, reliability, and sensitivity of motion correction strategies for resting-state functional MRI. *bioRxiv*.

[Patel et al., 2014] Patel, A. X., Kundu, P., Rubinov, M., Jones, P. S., Vértes, P. E., Ersche, K. D., Suckling, J., and Bullmore, E. T. (2014). A wavelet method for modeling and despiking motion artifacts from resting-state fMRI time series. *NeuroImage*, 95:287–304.

[Patriat et al., 2017] Patriat, R., Reynolds, R. C., and Birn, R. M. (2017). An improved model of motion-related signal changes in fMRI. *NeuroImage*, 144:74–82.

[Power et al., 2012] Power, J. D., Barnes, K. A., Synder, A. Z., Schlagger, B. L., and Petersen, S. E. (2012). Spurious but systematic correlations in functional connectivity MRI networks arise from subject motion. *NeuroImage*, 59(3):2142–2154.

[Power et al., 2014] Power, J. D., Mitra, A., Laumann, T. O., Snyder, A. Z., Schlaggar, B. L., and Petersen, S. E. (2014). Methods to detect, characterize, and remove motion artifact in resting state fMRI. *NeuroImage*, 84:320–341.

[Power et al., 2015] Power, J. D., Schlaggar, B. L., and Petersen, S. E. (2015). Recent progress and outstanding issued in motion correction resting state fmri. *NeuroImage*, 105:536–551.

[Pruim et al., 2015] Pruim, R. H., Mennes, M., van Rooij, D., Llera, A., Buitelaar, J. K., and Beckmann, C. F. (2015). ICA-AROMA: A robust ICA-based strategy for removing motion artifacts from fMRI data. *NeuroImage*, 112:267–277.

[Qu et al., 2016] Qu, Y., Liu, X., Zhuang, J., Chen, G., Mai, J., Guo, X., Ou, Y., Chen, J., Gong, W., Gao, X., Wu, Y., and Nie, Z. (2016). Incidence of Congenital Heart Disease: The 9-Year Experience of the Guangdong Registry of Congenital Heart Disease, China. *PLOS ONE*, 11(7):e0159257.

[Rahim et al., 2008] Rahim, F., Ebadi, A., Saki, G., and Remazani, A. (2008). Prevalence of Congenital Heart Disease in Iran: A Clinical Study. *Journal of Medical Sciences(Faisalabad)*, 8(6):547–552.

[Raichle et al., 2001] Raichle, M. E., MacLeod, A. M., Snyder, A. Z., Powers, W. J., Gusnard, D. A., and Shulman, G. L. (2001). A default mode of brain function. *Proceedings of the National Academy of Sciences*, 98(2):676–682.

[Roche et al., 1998a] Roche, A., Malandain, G., Ayache, N., and Pennec, X. (1998a). *Multimodal image registration by maximization of the correlation ratio*. PhD thesis, INRIA.

[Roche et al., 1998b] Roche, A., Malandain, G., Pennec, X., and Ayache, N. (1998b). The correlation ratio as a new similarity measure for multimodal image registration. *Proceedings of MICCAI*, pages 1115–1124.

[Rugg, 1917] Rugg, H. O. (1917). *Statistical methods applied to education: A textbook for students of education in the quantitative study of school problems*. Houghton Mifflin.

[Rutman, 2009] Rutman, M. S. (2009). Sedation for emergent diagnostic imaging studies in pediatric patients. *Current Opinion in Pediatrics*, 21(3):306–312.

[Salimi-Khorshidi et al., 2014] Salimi-Khorshidi, G., Douaud, G., Beckmann, C. F., Glasser, M. F., Griffanti, L., and Smith, S. M. (2014). Automatic denoising of functional MRI

data: Combining independent component analysis and hierarchical fusion of classifiers. *NeuroImage*, 90:449–468.

[Satterthwaite et al., 2013] Satterthwaite, T. D., Elliott, M. A., Gerraty, R. T., Ruparel, K., Loughead, J., Calkins, M. E., Eickhoff, S. B., Hakonarson, H., Gur, R. C., Gur, R. E., and Wolf, D. H. (2013). An improved framework for confound regression and filtering for control of motion artifact in the preprocessing of resting-state functional connectivity data. *NeuroImage*, 64(1):240–256.

[Satterthwaite et al., 2012] Satterthwaite, T. D., Wolf, D. H., Loughead, J., Ruparel, K., Elliott, M. A., Hakonarson, H., Gur, R. C., and Gur, R. E. (2012). Impact of In-Scanner Head Motion on Multiple Measures of Functional Connectivity: Relevance for Studies of Neurodevelopment in Youth. *NeuroImage*, 60(1):623–632.

[Saxena, 2005] Saxena, A. (2005). Congenital Heart Disease in India: A Status Report. *Indian Journal of Pediatrics*, 72(7):595–598.

[Shah et al., 2008] Shah, G., Singh, M., Pandey, T., Kalakheti, B., and Bhandari, G. (2008). Incidence of congenital heart disease in tertiary care hospital. *Kathmandu University Medical Journal*, 6(1):33–36.

[Shannon, 1948] Shannon, C. E. (1948). A Mathematical Theory of Communication. *Bell System Technical Journal*, 27(3):379–423.

[Smith et al., 2004] Smith, S. M., Jenkinson, M., Woolrich, M. W., Beckmann, C. F., Behrens, T. E. J., Johansen-berg, H., Bannister, P. R., Luca, M. D., Drobnjak, I., Flitney, D. E., Niazy, R. K., Saunders, J., Vickers, J., Zhang, Y., Stefano, N. D., Brady, J. M., and Matthews, P. M. (2004). Advances in functional and structural MR image analysis and implementation as FSL. *NeuroImage*, 23:208–219.

[Smyser et al., 2010] Smyser, C. D., Inder, T. E., Shimony, J. S., Hill, J. E., Degnan, A. J., Snyder, A. Z., and Neil, J. J. (2010). Longitudinal analysis of neural network development in preterm infants. *Cerebral Cortex*, 20(12):2852–2862.

[Smyser and Neil, 2015] Smyser, C. D. and Neil, J. J. (2015). Use of resting state functional MRI to study brain development and injury in neonates. *Seminars in Perinatology*, 39(2):130–140.

[TracInnovations, 2019] TracInnovations (2019). Tracinnovations mri markerless motion tracker and monitor system.

[United States Food and Drug Administration, 2016] United States Food and Drug Administration (2016). Drug Safety and Availability - FDA Drug Safety Communication: FDA review results in new warnings about using general anesthetics and sedation drugs in young children and pregnant women. Technical report, United States Food and Drug Administration.

[van der Linde et al., 2011] van der Linde, D., Konings, E. E., Slager, M. A., Witsenburg, M., Helbing, W. A., Takkenberg, J. J., and Roos-Hesselink, J. W. (2011). Birth Prevalence of Congenital Heart Disease Worldwide. *Journal of the American College of Cardiology*, 58(21):2241–2247.

[van der Maaten and Hinton, 2008] van der Maaten, L. and Hinton, G. (2008). Visualizing data using t-SNE. *Journal of Machine Learning Research*, 9(Nov):2579—-2605.

[van Dijk et al., 2012] van Dijk, K. R., Sabuncu, M. R., and Buckner, R. L. (2012). The influence of head motion on intrinsic functional connectivity MRI. *NeuroImage*, 59(1):431–438.

[Varoquaux, 2019] Varoquaux, G. (2019). K-means Clustering.

[Ward, 1963] Ward, J. H. . (1963). Hierarchical Grouping to Optimize an Objective Function. *Journal of the American Statistical Association*, 58(301):236–244.

[Waskom, 2018] Waskom, M. L. (2018). seaborn.clustermap.

[Webb et al., 2015] Webb, G., Mulder, B. J., Aboulhosn, J., Daniels, C. J., Elizari, M. A., Hong, G., Horlick, E., Landzberg, M. J., Marelli, A. J., O'Donnell, C. P., Oechslin, E. N., Pearson, D. D., Pieper, E. P., Saxena, A., Schwerzmann, M., Stout, K. K., Warnes, C. A., and Khairy, P. (2015). The care of adults with congenital heart disease across the globe: Current assessment and future perspective: A position statement from the International Society for Adult Congenital Heart Disease (ISACHD). *International Journal of Cardiology*, 195:326–333.

[Windram et al., 2011] Windram, J. D., Grosse-Wortmann, L., Shariat, M., Greer, M.-L., and Yoo, S.-J. (2011). The Feed and Sleep method: how to perform a cardiac MRI in the 1st year of life without the need for General Anesthesia. *Journal of Cardiovascular Magnetic Resonance*, 13(Suppl 1):P224.

[Woolrich et al., 2004] Woolrich, M. W., Behrens, T. E. J., Beckmann, C. F., Jenkinson, M., and Smith, S. M. (2004). Multilevel linear modelling for FMRI group analysis using Bayesian inference. *NeuroImage*, 21:1732–1747.

[Yan et al., 2013a] Yan, C. G., Cheung, B., Kelly, C., Colcombe, S., Craddock, R. C., Di Martino, A., Li, Q., Zuo, X. N., Castellanos, F. X., and Milham, M. P. (2013a). A comprehensive assessment of regional variation in the impact of head micromovements on functional connectomics. *NeuroImage*, 76:183–201.

[Yan et al., 2013b] Yan, C.-G., Craddock, R. C., He, Y., and Milham, M. P. (2013b). Addressing head motion dependencies for small-world topologies in functional connectomics. *Frontiers in Human Neuroscience*, 7(December):1–19.

[Zaitsev et al., 2017] Zaitsev, M., Burak, A., LeVan, P., and Knowles, B. R. (2017). Prospective Motion Correction in Functional MRI. *NeuroImage*, pages 33–42.

[Zaitsev et al., 2006] Zaitsev, M., Dold, C., Sakas, G., Hennig, J., and Speck, O. (2006). Magnetic resonance imaging of freely moving objects: prospective real-time motion correction using an external optical motion tracking system. *NeuroImage*, 31(3):1038–1050.

[Zang et al., 2007] Zang, Y. F., Yong, H., Chao-Zhe, Z., Qing-Jiu, C., Man-Qiu, S., Meng, L., Li-Xia, T., Tian-Zi, J., and Yu-Feng, W. (2007). Altered baseline brain activity in children with ADHD revealed by resting-state functional MRI. *Brain and Development*, 29(2):83–91.

[Zhao et al., 2019] Zhao, Q. M., Liu, F., Wu, L., Ma, X. J., Niu, C., and Huang, G. Y. (2019). Prevalence of Congenital Heart Disease at Live Birth in China. *Journal of Pediatrics*, 204:53–58.

[Zijdenbos et al., 1994] Zijdenbos, A. P., Dawant, B. M., Margolin, R. A., and Palmer, A. C. (1994). Morphometric Analysis of White Matter Lesions in MR Images: Method and Validation. *IEEE Transactions on Medical Imaging*, 13(4):716–724.

[Zou et al., 2004] Zou, K. H., Warfield, S. K., Bharatha, A., Tempany, C. M., Kaus, M. R., Haker, S. J., Wells, W. M., Jolesz, F. A., and Kikinis, R. (2004). Statistical Validation of Image Segmentation Quality Based on a Spatial Overlap Index. *Academic Radiology*, 11(2):178–189.